# Graphical Abstract

## Discovery of quasi-disordered truss metamaterials inspired by natural cellular materials

Akash Singh Bhuwal, Yong Pang, Ian Ashcroft, Wei Sun, Tao Liu

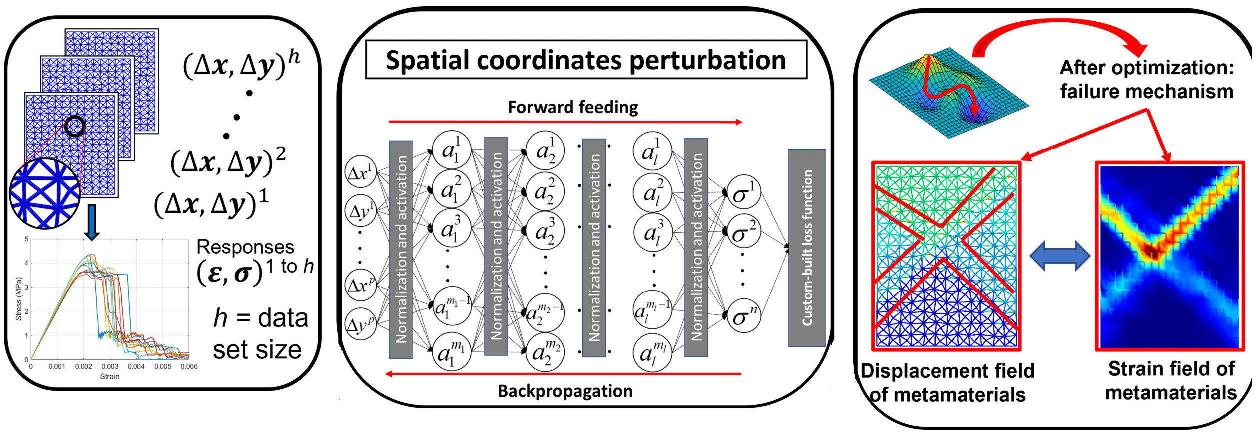

# Highlights

**Discovery of quasi-disordered truss metamaterials inspired by natural cellular materials**

Akash Singh Bhuwal, Yong Pang, Ian Ashcroft, Wei Sun, Tao Liu

- A combined deep-learning and global optimization algorithms have been used, to tune the distribution of the disorderliness to achieve damage-tolerant designs.
- Metamaterials created from a periodic Face Centered Cubic (FCC) lattice can achieve up to 100% increase in ductility at the expense of less than 5% stiffness and 8-15% tensile strength.
- The optimized metamaterial designs have shown a shear branching type failure mechanism to increase ductility.

# Discovery of quasi-disordered truss metamaterials inspired by natural cellular materials

Akash Singh Bhuwal[a], Yong Pang[a,c], Ian Ashcroft[b], Wei Sun[a], Tao Liu[a,c,d]

[a] *Composite Research Group, Faculty of Engineering, University of Nottingham, University Park, Nottingham, NG7 2RD, UK*
[b] *Centre for Additive Manufacturing, Faculty of Engineering, University of Nottingham, University Park, Nottingham, NG7 2RD, UK*
[c] *School of Engineering and Materials Science, Queen Mary University of London, Mile End Road, London, E1 4NS, UK*
[d] *e-mail: Tao.Liu@qmul.ac.uk*

**Abstract**

Natural cellular materials, such as marine mussels, honeycombs, woods, trabecular bones, plant parenchyma, sponges and protoreaster nodosus, may benefit from the disorderliness within their internal microstructures to achieve damage tolerant behaviors. Inspired by this, we have created quasi-disordered truss metamaterials (QTMs) via introducing spatial coordinate perturbations or strut thickness variations to the perfect, periodic truss lattices. Numerical studies have suggested that the QTMs can exhibit either ductile, damage tolerant behaviors or sudden, catastrophic failure mode, depending on the distribution of the introduced disorderliness. A data-driven approach has been developed, combining deep-learning and global optimization algorithms, to tune the distribution of the disorderliness to achieve the damage tolerant QTM designs. A case study on the QTMs created from a periodic Face Centered Cubic (FCC) lattice has demonstrated that the optimized QTMs can achieve up to 100% increase in ductility at the expense of less than 5% stiffness and 8-15% tensile strength. Our results suggest a novel design pathway for architected materials to improve damage tolerance.

*Keywords:* Metamaterials, Brittle to progressive failure, Artificial neural network

## 1. Introduction

Natural cellular materials, such as marine mussels, honeycombs, woods, trabecular bones, plant parenchyma, sponges and protoreaster nodosus, have inspired the development of mechanical metamaterials with desired or extreme mechanical properties (Figs. 1a-d) [1–8]. These include various truss-like micro-lattices, i.e., truss mechanical metamaterials, at a scale ranging from nanometres to millimetres, manufactured using various additive manufacturing techniques [9–11]. Truss metamaterials have provided unique opportunities to create lightweight structural components of high performance, such as lightweight sandwich structures [12, 13]. In addition, truss metamaterials are highly tailorable and can be designed to meet various multifunctional requirements, such as simultaneous load bearing, active cooling, and noise reduction [14, 15].

Up till now, the majority of the relevant research has focused on the truss mechanical metamaterials of highly ordered structures, i.e., the bulk metamaterial is formed by repeating a representative volume element (RVE) in the two-dimensional (2D) or the three-dimensional (3D) space [16, 17]. However, while nature-provided cellular materials resemble truss lattice structures of ordered, periodic arrangement, they are not perfectly periodic, and disorderliness has been observed in a wide range of natural cellular materials. Egmond, et al. [18] have suggested that natural cellular materials can incorporate disorderliness in combination with other mechanisms such as gradients. The gradients within natural cellular material can be seen as a gradual variation of the mechanical properties with dimensions, normally in accordance with a changing functional requirement. In this study, disorderliness is defined as a random variation of geometry affecting mechanical properties of the natural cellular materials. Egmond, et al. [18] have measured the disorderliness of the biological materials from trabecular bone to plant stems and fungi, using a disorder parameter $\dot{g}$ with $\dot{g} = 1$ representing the ordered system and $\dot{g} = 0.1$ the highly disordered system. They have identified the ranges of disorderliness within different types of biological materials, e.g. woods and fungi from $\dot{g} = 0.6$ to 0.8; trabecular bone and dentin from $\dot{g} = 0.55$ to 0.65; and corals and bee honeycomb from $\dot{g} = 0.9$ to 0.97 (see Fig. 1e).

The role of disorderliness in mechanical performance for natural cellular materials has not been fully understood yet. Existing research has suggested that introducing disorderliness to periodic cellular materials can cause a reduction in stiffness, strength, ductility, and fracture toughness [21–23]. However, Egmond, et al. [18] have recently found that the disorderliness at the range of $\dot{g} = 0.6$ to 0.8 within 2D Voronoi tessellation can cause an increase in toughness, through crack deflection, without loss of tensile strength in comparison with 2D regular hexagonal honeycombs. Based on this, they have hypothesized that structural disorder in natural cellular materials is a toughening mechanism and there may be a certain optimal degree of disorderliness in biogenic cellular materials in order to achieve damage tolerant behaviors. *Here, we hypothesize that not only the level of disorderliness but also the distribution of disorderliness within natural cellular materials may play an important role in achieving damage tolerance.* As we have shown in Figs. 1f-i, truss metamaterials with identical disorderliness can fail with either sudden, catastrophic brittle mode or progressive ductile mode during uniaxial tension tests, owing to the different distribution of disorderliness.

Structural materials of high performance are expected to have suitable ductility to (i) fail in a progressive manner that can give prior warning to failure events and (ii) have good load bearing capacity with the presence of flaws. It has been reported that highly ordered, periodic truss metamaterials often exhibit a sudden, catastrophic failure mode - when loaded beyond the yield point, localized bands of high strain emerge, causing catastrophic collapse [24–26]. To date, there are very limited studies on the design methodology to achieve damage tolerance for mechanical metamaterials. Owing to the highly nonlinear nature of the problems, the conventional finite element (FE) based design optimization methods are not efficient or even impractical for this purpose. Hence, mechanism-based design approaches have been attempted. Pham et al. [27, 28] have used the hardening mechanisms found in crystalline materials to develop damage-tolerant designs, primarily under compression. They have found that the disorderliness introduced to periodic truss metamaterials, by mimicking the microscale structure of crystalline materials such as grain boundaries, precipitates, and phases, can lead to the designs of progressive failure mode.

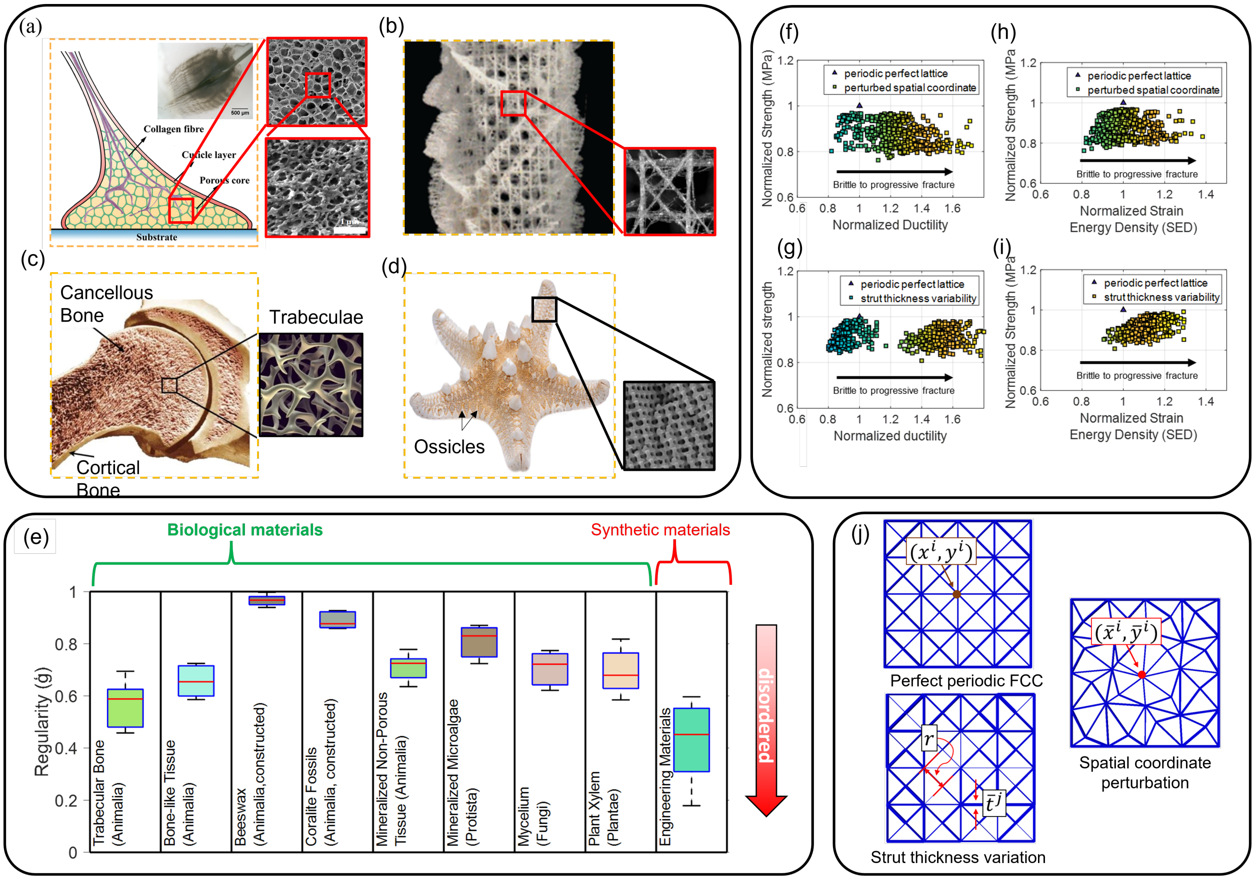


Figure 1: Natural cellular disordered metamaterials: (a) marine mussels on three different micro scales showing disorderliness of the struts [19], (b) deep-sea sponge, Euplectella aspergillum [3], consisting of square-grid-like architecture overlaid with a double set of diagonal bracing, (c) cortical and cancellous bone with trabeculae bone microstructure with porosity of 75% to 95% with naturally formed disorderliness [6, 20], (d) skeleton of protoreaster nodosus with its superficial soft tissue removed and SEM image of an ossicle's fracture surface affected by dislocation [8]; (e) disorderliness levels measured for all surveyed natural cellular materials (adapted from [18]); the effects of disorderliness on normalized strength versus ductility and strain energy density: (f & g) showing a wide range of ductility for spatial coordinate perturbation and strut thickness variation, respectively, (h & i) showing a wide range of strain energy density for spatial coordinate perturbation and strut thickness variation, respectively (j) creation of FCC QTMs via spatial coordinate perturbations and strut thickness variations.

Motivated by the hypotheses on the role of disorderliness in natural cellular materials, we here present a discovery framework for damage tolerant lattices via tuning the distribution of disorderliness to achieve damage tolerance. Our approach has focused on quasi-disordered truss metamaterials (QTMs), which were formed by introducing small disorderliness to (parent) periodic truss metamaterials. As reported by Wang and Sigmund [29], QTMs can be tailored to achieve the extreme maximum isotropic elastic property. Our results on the QTMs created from a periodic Face Centered Cubic (FCC) lattice have demonstrated that the optimized QTMs can achieve up to 100% increase in ductility at the expense of less than 5% stiffness and 8-15% tensile strength.

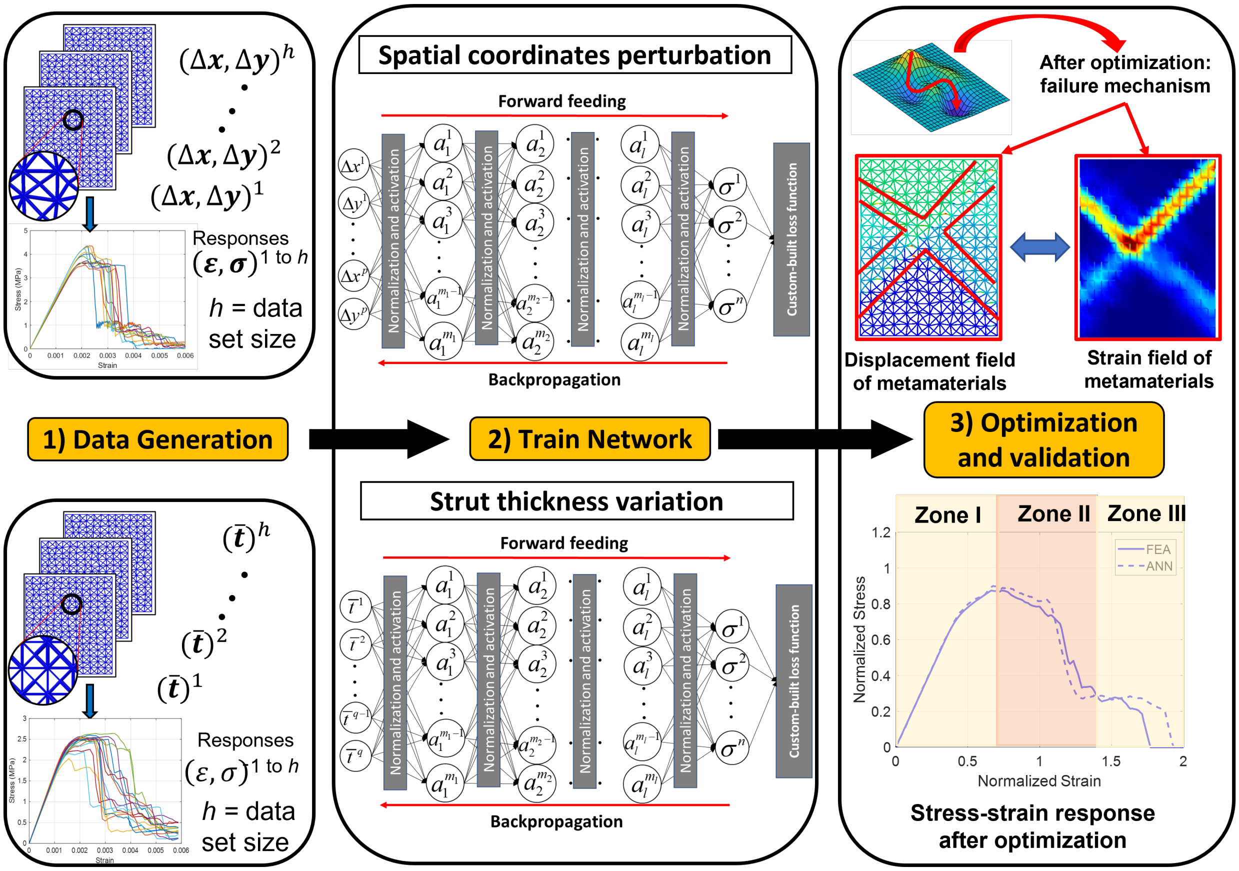


Figure 2: Overview of the methodology showing steps involved in designing QTMs, starting from step 1) data generation of spatial coordinate perturbation and strut thickness variation, step 2) ANN training with customised loss function to accurately map complex input and output variable, and step 3) optimization and validation of the designs.

## 2. Methodology

### *2.1. Creating the design space for quasi-disordered lattices*

Our approach to create QTMs of desired progressive failure modes was to introduce controlled (optimized) disorderliness to perfect periodic lattices of high performance. The periodic lattices with mechanical behavior close to the Hashin-Shtrikman (H-S) theoretical limit [16, 30, 31], such as Face Centred Cubic (FCC), triangular, and Kagome lattices [23], were chosen to act as the parent periodic lattices. Built upon data-driven approaches, the distribution and level of the disorderliness were tuned through optimization procedures to ensure that the desired progressive failure modes could be achieved with maintaining or without much loss of the good mechanical properties inherited from the parent periodic lattices. The geometries of the QTMs in the design space were numerically created through two distinct approaches, i.e., (1) random perturbation of the spatial coordinates of the nodes of a parent periodic lattice; and (2) random strut thickness variation of a parent periodic structure. Consider a two- dimensional (2D) parent periodic lattice with $(x^i, y^i)$ representing the spatial coordinates of the $i$th node and $t^j$ the thickness of $j$th strut. To create a QTM through random perturbation of the spatial coordinates of the nodes, the perturbation

$(\Delta x^i, \Delta y^i)$ was defined as [26]:

$$\begin{aligned} \Delta x^i &= \bar{x}^i - x^i = \beta\alpha r \\ \Delta y^i &= \bar{y}^i - y^i = \beta\alpha r \end{aligned} \tag{1}$$

Alternatively, to create a QTM through random strut thickness variation, the thickness of $j$th strut was defined as:

$$\bar{t}^j = (1 + \gamma\beta)t^j \tag{2}$$

In Eqs. 1 and 2, $\beta$ $(-1 \leq \beta \leq +1)$ denotes a random variable following a uniform distribution probability distribution; $r$ is the minimum distance between two nodes within the parent periodic lattice; $\alpha$ and $\gamma$ are the degrees of irregularity for the spatial perturbation and strut thickness variation, respectively. In this paper, small values are chosen for $\alpha = 0.2$ and $\gamma = 0.1$, which leads to QTMs with $\Delta x^i$ or $\Delta y^i \in [-0.2r, +0.2r]$ for spatial coordinate perturbation and $\bar{t}^j \in [-0.1t^j, +0.1t^j]$ for strut thickness variation. The method introduced in the paper can be extended to triangular/kagome parent geometries (see Appendix A, Fig. A.2 ).

### *2.2. A deep learning framework to map design space to output space*

The input and output databases were generated to feed into deep learning neural network for training purposes. The input database included the geometric information of the QTM samples. Let $h$ denote the number of QTM samples included in the input database, and each QTM has $p$ nodes and $q$ struts. As shown in Fig. 2, for the $m$th QTM sample, $m = 1, 2, \ldots, h$, the geometric information included in the input database consisted of (1) the perturbation of the spatial coordinates of the nodes, $(\Delta \boldsymbol{x}^m, \Delta \boldsymbol{y}^m)$, or (2) strut thickness variation, $\bar{\boldsymbol{t}}^m$, with

$$\Delta \boldsymbol{x}^m = \left[\Delta x^1, ..., \Delta x^p\right]^{m\ \mathrm{T}}, \ \Delta \boldsymbol{y}^m = \left[\Delta y^1, ..., \Delta y^p\right]^{m\ \mathrm{T}} \tag{3}$$

and

$$\bar{\boldsymbol{t}}^m = \left[\bar{t}^1, ..., \bar{t}^q\right]^{m\ \mathrm{T}} \tag{4}$$

The output database includes the information on the structural responses of the QTM samples obtained by finite element (FE) simulations (details of FE modelling have been given in Appendix B). As the current research focuses on the structural response under uniaxial tension, the normalized macroscopic stress data $\boldsymbol{\sigma}^m = [\sigma^1, \sigma^2, ..., \sigma^n]^{m\ \mathrm{T}}$ collected at a sequence of $n$ predefined, equally spaced normalized macroscopic uniaxial strains, $\boldsymbol{\varepsilon}^m = [\varepsilon^1, \varepsilon^2, ..., \varepsilon^n]^{m\ \mathrm{T}}$, were stored in the output database for the $m$th QTM sample. Here, the macroscopic tensile stresses are defined as the ratio of the applied tensile force by the cross-section area over which the force is applied (Appendix B, Eq. B.2); and the macroscopic tensile strain is defined as the elongation over the original length of the model (Appendix B, Eq. B.2).

A feed-forward deep-learning ANN was trained, using the input and output databases, to map the functional relationship between the input and output databases, as shown in Fig. 2, i.e.,

$$\boldsymbol{\sigma} = \left[\sigma^1, \sigma^2, ..., \sigma^n\right]^{\mathrm{T}} = f_1(\Delta\boldsymbol{x}, \Delta\boldsymbol{y}), \quad \text{or}$$
$$\boldsymbol{\sigma} = \left[\sigma^1, \sigma^2, ..., \sigma^n\right]^{\mathrm{T}} = f_2(\bar{\boldsymbol{t}}) \tag{5}$$

Neural network architecture refers to assembling neurons into layers: Each neuron uses a mathematical transformation of weights and biases to generate an output layer. For example, the mathematical form of a feed-forward propagation neural network of $l$ layers can be written as:

$$\begin{aligned}
&\boldsymbol{a}_1 = g\left(\boldsymbol{\theta}^{[1]}\boldsymbol{\psi} + \boldsymbol{b}_1\right)\\
&\boldsymbol{a}_2 = g\left(\boldsymbol{\theta}^{[2]}\boldsymbol{a}_1 + \boldsymbol{b}_2\right)\\
&\cdots\\
&\boldsymbol{a}_{ii} = g\left(\boldsymbol{\theta}^{[ii]}\boldsymbol{a}_{ii-1} + \boldsymbol{b}_{ii}\right)\\
&...\\
&\boldsymbol{a}_{l-1} = g\left(\boldsymbol{\theta}^{[l-1]}\boldsymbol{a}_{l-2} + \boldsymbol{b}_{l-1}\right)\\
&\boldsymbol{\sigma} = \boldsymbol{\theta}^{[l]}\boldsymbol{a}_{l-1} + \boldsymbol{b}_l
\end{aligned} \tag{6}$$

where $\boldsymbol{\theta}^{[ii]}$ is a weight matrix in the $ii$th layer, $ii = 1, 2, ..., l$; $\boldsymbol{b}_{[ii]}$ the bias vector in the $ii$th layer; $\boldsymbol{a}_{[ii]}$ the output vector in the $ii$th layer; $g$ the activation function; $\boldsymbol{\psi}$ is the input vector of the ANN, i.e.,

$$\boldsymbol{\psi} = \left[\left(\Delta x^1, \Delta y^1\right), ..., \left(\Delta x^p, \Delta y^p\right)\right]^{\mathrm{T}}, \quad \text{or}$$
$$\boldsymbol{\psi} = \bar{\boldsymbol{t}} = \left[\bar{t}^1, ..., \bar{t}^q\right] \tag{7}$$

The learning (training) procedure tunes the ANN components to minimise the cost function $J(\boldsymbol{\theta}^{[ii]}, \boldsymbol{b}_{ii})$, which is related to the loss function $\mathcal{L}(\boldsymbol{\sigma}^m_{pred}, \boldsymbol{\sigma}^m_{true})$, by the following Equation [32]:

$$J(\boldsymbol{\theta}^{[ii]}, \boldsymbol{b}_{ii}) = \frac{1}{h}\sum_{m=1}^{h}\mathcal{L}(\boldsymbol{\sigma}^m_{pred}, \boldsymbol{\sigma}^m_{true}) \tag{8}$$

where the loss function measures the accuracy of the trained ANN by evaluating the difference between the predicted stresses, $\boldsymbol{\sigma}^m_{pred} = [\sigma^1, \sigma^2, ..., \sigma^n]^{m\ \mathrm{T}}_{pred}$ and the real stresses, $\boldsymbol{\sigma}^m_{true} = [\sigma^1, \sigma^2, ..., \sigma^n]^{m\ \mathrm{T}}_{true}$.

To improve the learning efficiency of the ANN model, the normalized macroscopic stress data $\boldsymbol{\sigma}^m = [\sigma^1, \sigma^2, ..., \sigma^n]^{m\ \mathrm{T}}$ for a QTM sample can be divided into three groups, which correspond to the three zones in the stress-strain relation for the QTM sample under uniaxial tension, respectively, as shown in Fig. 2. It is noted that the structure experiences (1) elastic deformation in Zone I, (2) plastic deformation caused by the failure of a limited number of struts in Zone II, and (3) final catastrophic failure in Zone III. Numerical experiments on quasi-disordered FCC lattices have suggested that the stress data in the three groups (Zones) have significantly different variances across the QTM samples (see Appendix C.2 Fig. C.2). Based on this finding, a novel quantile regression loss function has been employed in this work, which is given as:

$$\mathcal{L}_{custom}(\boldsymbol{\sigma}^k_{pred}, \boldsymbol{\sigma}^k_{true}) = \frac{1}{3n}\sum_{i=1}^{3}\left[\sum_{\substack{k=1\\ \sigma^k_{true}<\sigma^k_{pred}}}^{n} (\lambda_i - 1)\left(\sigma^k_{pred} - \sigma^k_{true}\right)^2 + \sum_{\substack{\mathrm{k=1}\\ \sigma^k_{true}\geq\sigma^k_{pred}}}^{n} \lambda_i\left(\sigma^k_{pred} - \sigma^k_{true}\right)^2\right] \tag{9}$$

where $\lambda_i$, $i = 1, ..., 3$, are the chosen quantiles for the three groups of the stress data and have values between 0 and 1. The quantile loss function is an extension of the Mean Square Error (MSE) that has the quantile $\lambda_i = 0.5$. The larger the value $\lambda_i$, the more under-predictions are penalized than over-predictions. Our numerical experiments have suggested that it can help to improve deep-learning efficiency (see Appendix C.5) and reduce the amount of data required for the deep-learning process by using distinct $\lambda_i$ values at different Zones.

### *2.3. Non-gradient-based design optimization*

Design optimization procedures can be employed to tune the distribution of disorderliness within the parent periodic lattices to achieve desired progressive failure modes. The mathematical model for design optimization can be described as follows:

**Objective function (maximize):**

$$T(\Delta\boldsymbol{x}, \Delta\boldsymbol{y}) \text{ Or } T(\bar{\boldsymbol{t}}) \tag{10}$$

**Constraints:**

$$\begin{aligned}
&\Delta x_{\min} \leq \Delta x^i \leq \Delta x_{\max};\\
&\Delta y_{\min} \leq \Delta y^i \leq \Delta y_{\max}, \quad i \in [1, p]\\
&\text{or}\\
&t_{\min} \leq \bar{t}^j \leq t_{\max}, \quad j \in [1, q]\\
&\text{and}\\
&\langle \sigma_{ut} \rangle \geq \sigma_{\min}\\
&\langle E_0 \rangle \geq E_{0\,\min}
\end{aligned} \tag{11}$$

where $\langle \sigma_{ut} \rangle$ and $\langle E_0 \rangle$ denote the maximum normalized macroscopic tensile stress and the macroscopic Young's modulus of the lattice obtained by the uniaxial tensile tests, respectively; $\Delta x_{\min}$, $\Delta y_{\min}$, $t_{\min}$, $\sigma_{\min}$ and $E_{0\,\min}$ are the lower bounds of design variables; and $\Delta x_{\max}$, $\Delta y_{\max}$ and $t_{\max}$ the upper bounds. In Eq. 10, the objective function $T$ is a measurement related to the deformation capacity of the QTMs, such as ductility and strain energy density obtained under uniaxial tensile load. Here and throughout the rest of the paper, the ductility is defined as the macroscopic tensile strain at failure, which corresponds to the post-peak macroscopic stress equivalent to 25% of the peak macroscopic tensile stress; and the strain energy density was calculated as the area under the macroscopic stress-strain curve.

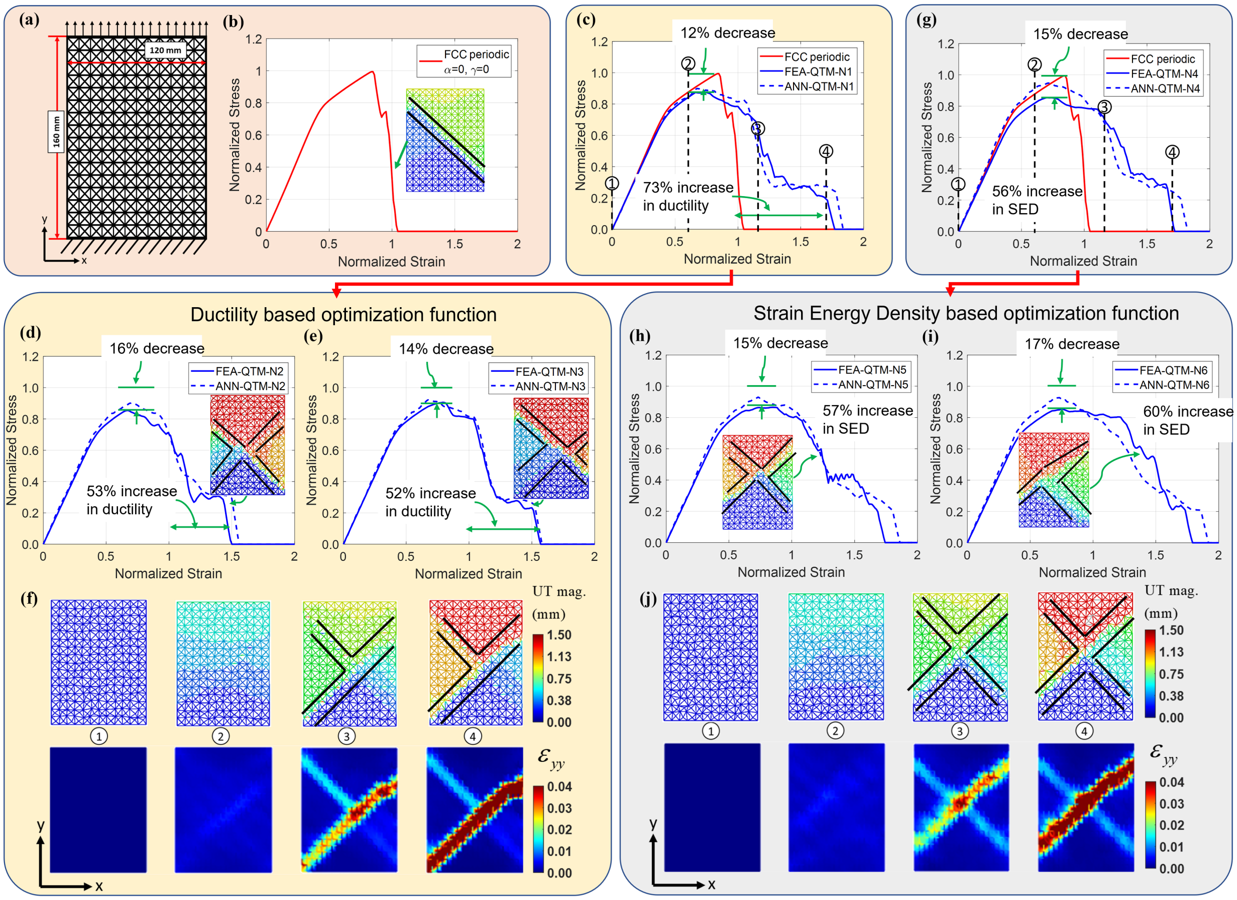


Figure 3: Designs of metamaterials based on spatial coordinate perturbations (a) the dimensions and boundary conditions of the FE model; (b) the normalized macroscopic stress-strain relation of a parent periodic FCC lattice; (c, d and e) the normalized stress-strain curves of three optimized QTMs (-N1, -N2 and -N3, using ductility objective function) obtained by the FE simulations and ANN predictions; (f) the detailed distributions of displacements in the lattices along with the continuum plots of microscopic strain [26] at selected macroscopic strains of a QTM (-N1), showing shear band branching; the corresponding results of the three QTMs (-N4, -N5 and -N6) obtained using strain energy density objective function are shown in (g, h, i and j). The inserts of (d, e, h and i) show the distribution of the displacement at failure, which is caused by the formulation of the shear band branching with different patterns.

## 3. Results and Discussions

We demonstrate the success of the proposed method through the discovery of the high-performance 2D QTMs of the progressive failure modes. The QTMs were created based on a parent periodic FCC lattice (Appendix A). It was assumed that the lattice was made of the aluminium alloy Al-1050A, and with relative density, $\bar{\rho} = 0.2$. This relative density value was chosen for our investigation while taking the manufacturability of the minimum strut thickness into consideration [25]. The parent periodic FCC lattice consisted of 12- and 16-unit cells periodically arranged along the $x$ and $y$ directions, respectively, with dimensions of 120 mm in $x$ direction and 160 mm in $y$ directions, see Fig. 3a. This geometry was chosen to ensure that the mechanical properties, i.e., macroscopic stiffness and peak strength were not sensitive to the size of the test samples (Appendix D). The FE simulations have suggested that the parent lattice exhibits a sudden, catastrophic structural failure mode under uniaxial tension along the direction, as shown in Fig. 3b for the corresponding normalized macroscopic stress-strain relation. As shown in the insert of Fig. 3b for the distribution of the displacement at failure, the failure event was mainly caused by the formulation of a single shear band across the sample. For the macroscopic stress-strain relation shown in Fig. 3b and the rest of the paper, the stress values have been normalized by the peak stress, and the strain values by the maximum strain of the parent FCC periodic lattice.

### *3.1. The ANN models*

The first ANN model was created based on the scenario in which disorderliness was introduced into the FCC periodic lattice via the perturbation of the spatial coordinates of the nodes. The geometries of 5000 QTM samples were generated with irregularity, $\alpha = 0.2$, at constant relative density, $\bar{\rho} = 0.2$. The input database containing perturbation of the spatial coordinates of the nodes, $\boldsymbol{\psi} = \left[\left(\Delta x^1, \Delta y^1\right), ..., \left(\Delta x^p, \Delta y^p\right)\right]^{\mathrm{T}}$, and the output database containing the normalized macroscopic stress data, $\boldsymbol{\sigma} = \left[\sigma^1, \sigma^2, ..., \sigma^n\right]^{\mathrm{T}}$, were created to train the ANN model. The ANN model consisted of 7 hidden layers with 4096, 2048, 1024, 1024, 1024, 512, and 512 neurons, respectively, in sequence from input to output layers. The numerical experiments have suggested that the structure of the ANN has achieved high efficiency in deep learning. The tuning of ANN model hyperparameters was obtained by performing Bayesian Optimization (Appendix C.4), based on the loss function with ($\lambda_1 = 0.5, \lambda_2 = 0.45$ and $\lambda_3 = 0.1$), respectively. The second ANN model was created based on the scenario in which the disorderliness was introduced into the parent FCC periodic lattice via strut thickness variation. The ANN model was trained based on the input database containing struct thicknesses, $\boldsymbol{\psi} = \bar{\boldsymbol{t}} = [\bar{t}^1, ..., \bar{t}^q]$, and the output database resulted from the FE simulations for 5000 QTM samples, with irregularity $\gamma = 0.1$ and at constant relative density, $\bar{\rho} = 0.2$. The ANN parameters are the same as in the previous case, except that the chosen quantiles were $\lambda_1 = 0.5, \lambda_2 = 0.5$ and $\lambda_3 = 0.3$, respectively. We trained the two ANN models for 1000 iterations with an early stopping function when no improvements were made for ten iterations consecutively (the evaluations on the full dataset are presented in Appendix C.5).

### *3.2. The design optimization*

The optimization problem described in Eqs. 10 and 11 can be solved using non-gradient based optimization algorithms, such as the Genetic Algorithms [33, 34], the Particle Swarm Optimization [35], and the Simulated Annealing (SA) Optimization [36], with the structural responses calculated by finite element (FE) simulations.

The objective functions were optimized with the constraints of allowable nodal perturbation, $\alpha = 0.2$, allowable struct thickness variation $\gamma = 0.1$, minimum normalized strength, $\sigma_{\min} = 0.9$, and minimum normalized stiffness, $E_0 = 0.95$, using the simulated annealing (SA) optimization algorithm (MATLAB [37]). However, owing to the highly nonlinear nature of the problem, we found that it was impractical to use the FE based optimization procedures to solve the optimization problem. A numerical experiment suggested that it took up to 7 minutes to calculate the structural response of a single sample under a uniaxial tensile test. In this work, we used the simulated annealing (SA) optimization algorithm to achieve the optimized designs with the upper limit of 10000 iterations. As shown in Table

1, under the environment of the PC with Intel(R) Core(TM) i5-5200U CPU @ 2.20GHz, 4 core processors with 16GB RAM, it took approximately 0.015 minutes to complete a single calculation by a trained ANN model, compared to 7-15 minutes by a single FE calculation (up to 48 days for the optimization process). Hence, ANN based optimization process is far more efficient than the conventional FE based optimization process.

Table 1: Quantitative comparison of the FEA versus the ANN based optimization method time

| number of samples | FEA based optimization (min) | ANN based optimization (min) |
|---|---|---|
| 1 | ∼7-15 | 0.015 |
| 5000(FE - actual) | ∼54100 | ∼54100 (ANN database) |
| 10000(extrapolated) | ∼108200 (∼75 days) | 150 |

The strength constraint can ensure that the resulted QTMs preserve more than 90% of the strength and 95% of the stiffness from the parent periodical FCC lattice. The relative density of optimized QTMs have been found to be maintained at a constant value $\bar{\rho} = 0.2$. The optimization results are presented below for the QTMs having improved ductility owing to the progressive failure process.

### *3.3. The Optimized results*

Based on the first ANN model, we optimized the distribution of the perturbation of the spatial coordinates of the nodes for the maximized ductility design and the maximized strain energy density design, respectively, as shown in Fig. 3 for the optimized designs. The optimized distributions of the nodal perturbation were used to create the corresponding FE models for validation and interpretation purposes. Compared to the periodic FCC lattice (Fig. 3b), which failed in a sudden, catastrophic manner, the optimized designs exhibited progressive failure modes. The optimized design based on the maximized ductility design model exhibits a 73% increase in ductility (Fig. 3c); and the optimized design based on the maximized strain energy density model exhibits a 56% increase in strain energy density (Fig. 3g), both with less than 5% reduction in stiffness and up to 15% reduction in strength. The ANN predictions have good agreement with the FE simulation results. FE simulations suggested that the progressive failure modes in the optimized designs were mainly achieved by shear band branching that causes load-path shift to undamaged struts, as shown in Fig. 3f (QTM-N1) and Fig. 3j (QTM-N4) for ductility and strain energy density objective functions, respectively. However, it has been found that the optimized designs were not unique: the solution is sensitive to the initial distribution of the perturbation. This indicates that the method can generate different designs with similar local optima. To illustrate this, based on three different initial distributions that were randomly picked from the input dataset, we obtained the optimized distributions of the perturbation for the maximized ductility designs (Figs. 3c, d and e for QTMs-N1, -N2 and -N3) and the maximized strain energy density designs (Figs. 3g, h and i for QTMs-N4, -N5 and -N6), respectively. Albeit slight differences in mechanical behaviors, these optimized designs all show progressive failure modes with a significant increase in ductility or strain energy density compared to the periodic FCC lattice. The inserted distribution of the displacement at failure, as shown in Figs. 3d, e, f and Figs. 3h, i, j, have suggested that the progressive failure modes were mainly caused by shear band branching in different patterns.

In this section, we optimized the variation of strut thickness within the parent periodic FCC lattices using the ductility objective function, as shown in Fig. 4 for the three optimized designs. As in the previous case, we obtained the optimum designs that exhibited progressive failure modes compared to the periodic FCC lattice (Fig. 3a). The optimized designs exhibit more than 80% increase in ductility with the expense of less than 5% stiffness and less than 11% strength (Figs. 4a, b and c); and again the progressive failure modes in the optimized designs were mainly achieved by the shear band branching with different patterns, as shown in Fig. 4b, c and d of QTMs -S1, -S2 and -S3. Similarly, we have obtained three optimized QTM designs using the strain energy density objective function, as shown in Fig. 4. The optimized designs exhibit more than 60% increase in strain energy density with the expense of less than 5% stiffness and less than 9% strength (Figs. 4e, f and g). Our results show that the QTMs resulting from the strut thickness variation are more prone to brittle failure compared to those resulting from the spatial nodal perturbation. It can be noted that, for both models, i.e., the spatial coordinate perturbation and strut thickness variation, the number of variables in the input vector for the ANN models and optimization are different. However, our numerical experiments suggest that the difference in computation time is not noticeable.

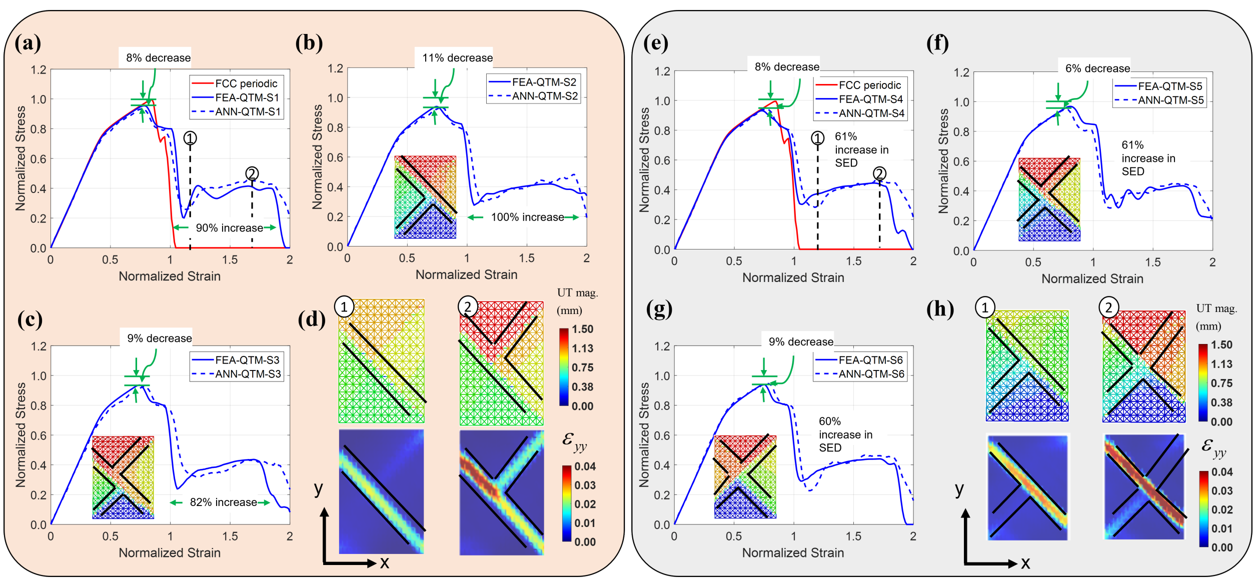


Figure 4: Designs of metamaterials based on strut thickness variation using ductility objective function, (a, b and c) the normalized stress-strain curves of three optimized QTMs (-S1, -S2 and -S3) obtained by the FE simulations and ANN predictions; (d) the distribution of microscopic strain at selected macroscopic strains of a QTM (-S1), showing that shear band branching causes progressive failure mode; the corresponding results of the three QTMs (-S4, -55 and -S6) obtained using strain energy density objective function is shown in (e, f, g and h). The inserts of (b, c, f and g) show the distribution of the displacement at failure, which is caused by the formulation of the shear band branching with different patterns.

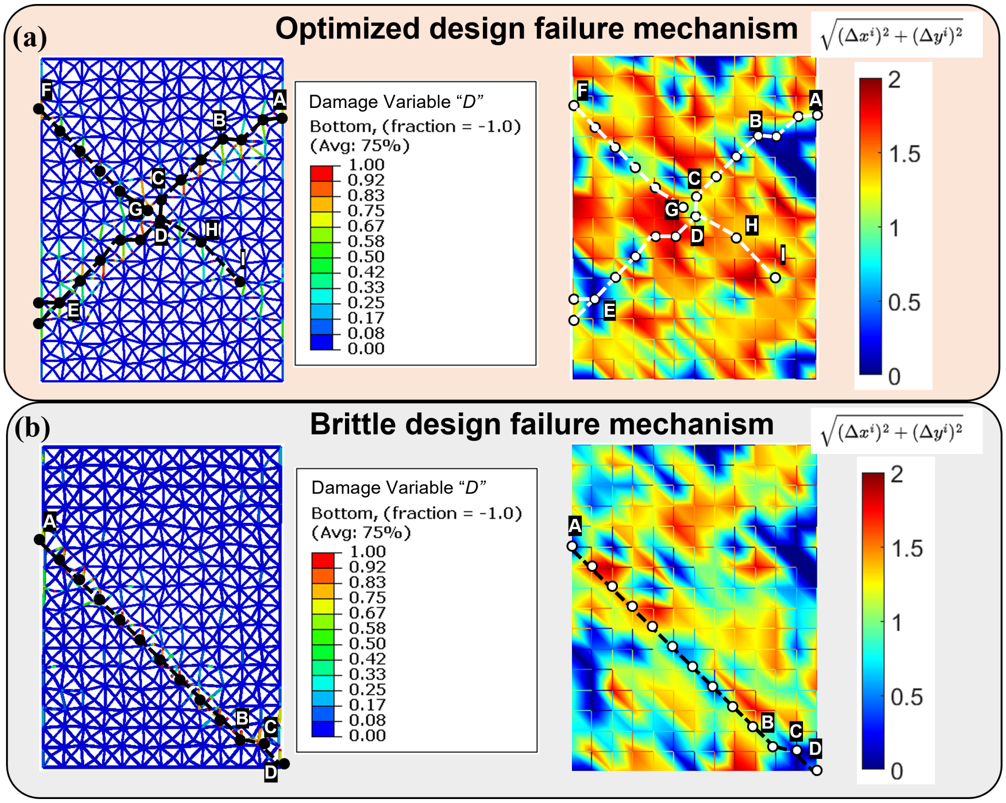


Figure 5: Failure mechanisms of two QTM designs: (a) an optimized QTM-N3 (b) a randomly selected low ductile QTM with brittle fracture

### *3.4. Failure mechanism*

To understand how initial disorderliness can affect shear band branching that leads to enhancement of ductility, we have studied the failure mechanisms of two QTM designs: i) an optimized QTM with improved ductility (Fig. 5a), and ii) a QTM with low ductility brittle failure mode (Fig. 5b). The failure paths have been traced for both designs, which were caused by the breaking of struts owing to damage, as shown in the detailed geometries of the QTMs with contour showing the magnitude of the damage variable $D$. Here, the damage variable $D$ varies from 0 to 1, with $D = 1$ representing complete failure at the integration point of the element. The resultant initial spatial coordinate perturbation, i.e., $\sqrt{(\Delta x^i)^2 + (\Delta y^i)^2}$, is employed to quantify the overall disorderliness at $i$th node. The continuum plots of the resultant coordinate perturbations suggest that the optimized QTM (Fig. 5a) has a higher level distribution of disorderliness than the brittle QTM (Fig. 5b). For both QTMs, the failure paths were initiated at the locations with a low level of disorderliness. For the optimized QTM (Fig. 5a), the breaking of struts was initiated at Point A and followed the path with minimum disorderliness, i.e., Points B and C for the formulation of a shear band; near Point C when the shear band encountered highly distorted area, shear band branching occurred and multiple shear bands started to formulate. In contrast, for the brittle QTM (Fig. 5b), the shear band branching did not occur owing to the absence of a highly distorted area on the failure path.

## 4. Experimental Study

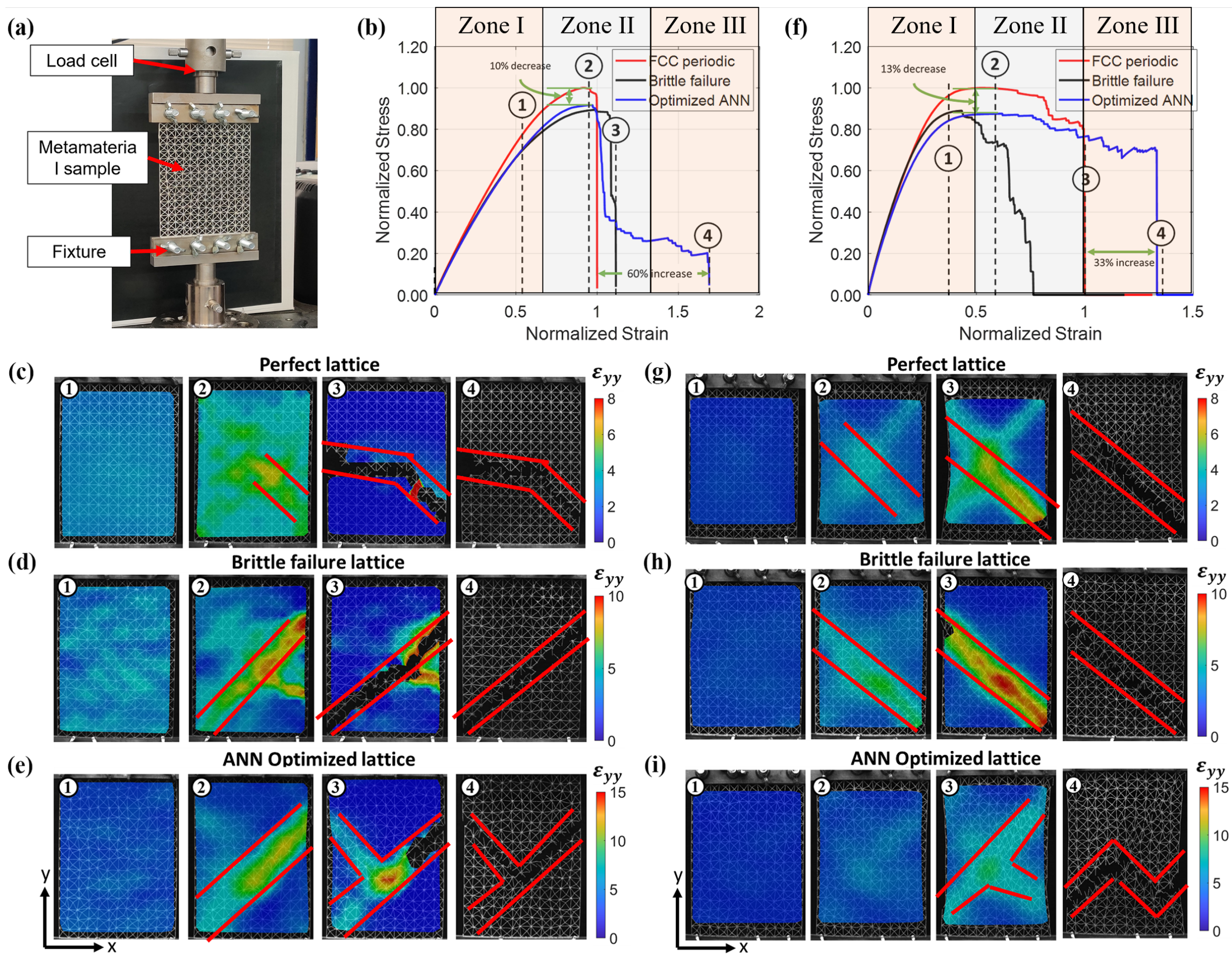


Figure 6: Tensile tests of the parent periodic FCC lattice, the QTM with progressive failure mode (QTM-1), and the QTM with sudden failure mode (QTM-2). (a) 3D printed QTM-1 using *polymer1* sample and experimental setup, (b) the normalized stress-strain curves of QTM-1 showing 60% increase in ductility using *polymer1*, (c), (d) and (e) snapshots of *polymer1* samples at different global strains during the test of parent periodic FCC, QTM-2, and QTM-1, respectively. The DIC images show the progression of microscopic strain $\varepsilon_{yy}$ and shear band branching (f) the normalized stress-strain curves of QTM-1 showing 33% increase in ductility using *polymer2*, (g), (h) and (i) are snapshots at different global strains for *polymer2*. (the fourth snapshots of parent periodic FCC lattice, QTM-1 and QTM-2 were taken after the final fracture occurred)

To validate the methodology described above, test specimens were manufactured, using the PolyJet manufacturing technique via an Objet260 Connex 3D printer, for the uniaxial tension test based on three selected FCC lattice designs, i.e., the parent periodic FCC lattice, the QTM with progressive failure mode (QTM-1), and the QTM with sudden failure mode (QTM-2). The optimized design shown in Fig. 3j was used as the geometry of the QTM-1; and the geometry of the QTM-2 was selected from the data used for deep learning, which exhibited sudden catastrophic failure mode according to the FE simulations. As discussed for the failure mechanism, the shear band branching was mainly caused by the distribution of initial disorderliness. To question if the enhancement in damage tolerance depends on the parent material of the lattices, we chose polymers as the parent material instead of Aluminum alloy (Al1050A), which was used in the design optimization as described previously. Two types of polymers (i.e., *polymer1* and *polymer2*) were used as the parent materials, which were created by combining commercialized acrylic (Objet Vero-Clear FullCure810) and rubber-like material (Objet Tango-Gray FullCure950). *Polymer1* has a mixture of 75% acrylic and 25% rubber-like material, and *polymer2* has a mixture of 50% acrylic and 50% rubber-like material. Both polymers show elastic-plastic stress-strain response, with *polymer2* being much more ductile than *polymer1* (see Appendix E). The tensile tests were conducted at room temperature using a 0.1% strain rate using an INSTRON testing system, as shown in Fig. 6a for a photograph of the experimental setup. Each specimen contained $12 \times 16$ cells, and the geometry of the specimen had size $120 \times 160$ mm (with a height of 25mm clamping at both top and bottom sides) with 1 mm out-of-plane thickness, and each strut had 0.4 mm thickness (the detailed geometry of the experimental sample is presented in Appendix E). Digital image correlation (DIC) was employed to capture the full-field strain evolution of the samples during the full fracture process. A CCD camera (Thorlabs DCC1545M) with an imaging lens (100mm focal length) was configured at a spatial resolution of 5 pixels/mm and a frame rate of 20 fps. In the DIC algorism, the subset image was $128 \times 128$ pixels, and the step size was 64 pixels to maintain a high level of speckle correlation [38, 39].

The normalized macroscopic stress-strain curves for the specimens made of *polymer1* and *polymer2* are shown in Figs. 6b and f, respectively. For both parent materials, the periodic FCC lattice failed in a sudden, catastrophic manner. Compared to the periodic FCC lattice, the QTM-1 achieved a 60% increase in ductility for *polymer1* and a 33% increase for *polymer2*, respectively, without significantly decreasing the mechanical stiffness ($\leq 3\%$) and the strength ($\leq 13\%$). On the other hand, for both parent materials, the QTM-2 exhibited sudden, catastrophic failure mode with ductility either slightly higher (*polymer1*) or much lower (*polymer2*) than that of the periodic FCC lattice. The three Zones shown in Figs. 6b and f, indicate that the increase in ductility mainly affected by the Zone III for *polymer1* or both Zone II and Zone III for *polymer2*.

To further examine the failure mechanisms, a series of video snapshots at four selected tensile strains, numbered as “1”, “2”, “3” and “4” shown in Figs. 6b and f, were presented in Fig. 6c-e (*polymer1*) and Figs. 6g-i (*polymer2*), respectively. For both parent polymers, both the periodic FCC structure and QTM-2 fail instantaneously owing to a single shear band formation across the sample at the tensile strain “3”. Interestingly, the shear band deflection in Fig. 6c did not lead to progressive failure mode owing to the brittle parent material (*polymer1*). On the other hand, the QTM-1 design develops damage-tolerant behaviors via progressive failure modes owing to shear band branching (Fig. 6e, *polymer1*) or excessive tortuosity in the development of the shear band (Fig. 6i, *polymer2*).

## 5. Conclusions

The structures of the natural cellular materials exhibit a certain level of disorderliness. Prior to this work, it was well established that the disorderliness within cellular materials can cause a reduction in stiffness, strength, ductility, and fracture toughness. This has been demonstrated by a range of theoretical and experimental studies by Romijn et al. [21], Chen et al. [22], Tankasala et al. [23], and Xu et al. [40]. However, in this paper, we have shown that the level and the distribution of disorderliness can either increase or decrease ductility of the truss lattice metamaterials by a great margin (see Figs. 1f and g), affecting both stiffness and strength. With this continuation, we have developed a physical-based data-driven framework, which tunes the disorderliness to achieve the QTMs with improved ductility. The higher ductility was achieved through changing the failure mechanisms from single shear band formulation to shear band branching or excessive shear tortuosity, which led to desired progressive failure modes. We have shown that, the solutions from the optimization calculation are not unique, which suggests that there are more than one optimum distribution of the disorderliness, however, they have all utilized progressive failure modes to improve the ductility. With this data-driven methodology, we can achieve the designs with ductility increased up to 100% without losing much of their stiffness ($< 5\%$) and strength ($8 \sim 15\%$). Our numerical study has benefited from well-designed ANN deep-learning models, built upon a custom-built loss function (Appendix C.5, Fig. C.3), which can be trained with a relatively small dataset. Additionally, we have used two different types of polymers as the parent material in the experimental study, which have demonstrated that the enhanced damage tolerant behaviors of the optimized metamaterials are material independent.

The design of damage-tolerant mechanical metamaterials [27] has significant importance in engineering applications. However, no deterministic approaches were developed prior to this work due to the indefinite solutions available. We believe this is just a beginning of an exciting field in the novel topological designs of mechanical metamaterials with tailored properties. Although the examples shown in the result section is based on FCC lattices, it is essential to note that the mechanical behaviors of other types of truss lattice such as Kagame, Diamond and Triangular, may differ from the FCC based lattices. It is likely that the difference in deformation mechanisms, i.e., bending dominated or stretching dominated, and redundancies of lattice structures [41] may lead to different damage tolerant behaviors with the presence of disorderliness. Future work will be conducted to reveal the underlying mechanisms via comparing different type of lattice structures. This study opens a new research area in seeking damage tolerance metamaterials, and the proposed method is general and applicable to other truss lattice topologies at any scale. The approach proposed in this paper can undoubtedly serve as a unique tool for designing novel mechanical metamaterials well beyond elastic limits.

## Acknowledgments

The authors acknowledge the financial support from the Leverhulme Trust through Research Grant Scheme (RPG-2020-235) and the University of Nottingham for the Dean of Engineering Research Scholarship for International Excellence, UK for Akash Bhuwal.

## References


[1] Z. Qin, M. J. Buehler, Impact tolerance in mussel thread networks by heterogeneous material distribution, Nature Communications (2013). doi:10.1038/ncomms3187.

[2] P. Van Liedekerke, E. Tijskens, H. Ramon, P. Ghysels, G. Samaey, D. Roose, Particle-based model to simulate the micromechanics of biological cells, Physical Review E - Statistical, Nonlinear, and Soft Matter Physics (2010). doi:10.1103/PhysRevE.81.061906.

[3] M. C. Fernandes, J. Aizenberg, J. C. Weaver, K. Bertoldi, Mechanically robust lattices inspired by deep-sea glass sponges, Nature Materials (2021). doi:10.1038/s41563-020-0798-1.

[4] T. M. Ryan, C. N. Shaw, Trabecular bone microstructure scales allometrically in the primate humerus and femur, Proceedings of the Royal Society B: Biological Sciences (2013). doi:10.1098/rspb.2013.0172.

[5] K. Ando, H. Onda, Mechanism for deformation of wood as a honeycomb structure I: Effect of anatomy on the initial deformation process during radial compression, Journal of Wood Science (1999). doi:10.1007/BF01192328.

[6] A. M. Torres, A. A. Trikanad, C. A. Aubin, F. M. Lambers, M. Luna, C. M. Rimnac, P. Zavattieri, C. J. Hernandez, Bone-inspired microarchitectures achieve enhanced fatigue life, Proceedings of the National Academy of Sciences of the United States of America (2019). doi:10.1073/pnas.1905814116.

[7] H. S. Gupta, J. Seto, W. Wagermaier, P. Zaslansky, P. Boesecke, P. Fratzl, Cooperative deformation of mineral and collagen in bone at the nanoscale, Proceedings of the National Academy of Sciences of the United States of America (2006). doi:10.1073/pnas.0604237103.

[8] T. Yang, H. Chen, Z. Jia, Z. Deng, L. Chen, E. M. Peterman, J. C. Weaver, L. Li, A damage-tolerant, dual-scale, single-crystalline microlattice in the knobby starfish, Protoreaster nodosus, Science 375 (6581) (2022) 647–652. doi:10.1126/science.abj9472.

[9] X. Zheng, H. Lee, T. H. Weisgraber, M. Shusteff, J. DeOtte, E. B. Duoss, J. D. Kuntz, M. M. Biener, Q. Ge, J. A. Jackson, S. O. Kucheyev, N. X. Fang, C. M. Spadaccini, Ultralight, ultrastiff mechanical metamaterials, Science (2014). doi:10.1126/science.1252291.

[10] T. A. Schaedler, A. J. Jacobsen, A. Torrents, A. E. Sorensen, J. Lian, J. R. Greer, L. Valdevit, W. B. Carter, Ultralight metallic microlattices, Science (2011). doi:10.1126/science.1211649.

[11] P. Fratzl, J. W. C. Dunlop, R. Weinkamer, Materials Design Inspired by Nature: Function Through Inner Architecture, 2013.

[12] T. Liu, Z. C. Deng, T. J. Lu, Design optimization of truss-cored sandwiches with homogenization, International Journal of Solids and Structures (2006). doi:10.1016/j.ijsolstr.2006.04.010.

[13] T. Liu, Z. C. Deng, T. J. Lu, Minimum weights of pressurized hollow sandwich cylinders with ultralight cellular cores, International Journal of Solids and Structures (2007). doi:10.1016/j.ijsolstr.2006.09.018.

[14] Z. Jia, F. Liu, X. Jiang, L. Wang, Engineering lattice metamaterials for extreme property, programmability, and multifunctionality (2020). doi:10.1063/5.0004724.

[15] T. Liu, Z. C. Deng, T. J. Lu, Bi-functional optimization of actively cooled, pressurized hollow sandwich cylinders with prismatic cores, Journal of the Mechanics and Physics of Solids (2007). doi:10.1016/j.jmps.2007.04.007.

[16] J. B. Berger, H. N. G. Wadley, R. M. McMeeking, Mechanical metamaterials at the theoretical limit of isotropic elastic stiffness, Nature 543 (7646) (2017) 533–537. doi:10.1038/nature21075.

[17] T. Tancogne-Dejean, M. Diamantopoulou, M. B. Gorji, C. Bonatti, D. Mohr, 3D Plate-Lattices: An Emerging Class of Low-Density Metamaterial Exhibiting Optimal Isotropic Stiffness, Advanced Materials (2018). doi:10.1002/adma.201803334.

[18] D. A. Egmond, B. Yu, S. Choukir, S. Fu, G. H. , C.V. Singh, B. Hatton, The benefits of structural disorder in natural cellular solids, Applied Physics (physics.app-ph); Materials Science (cond-mat.mtrl-sci) (2021). arXiv:/arxiv.org/abs/2110.04607v1, doi:https://doi.org/10.48550/arXiv.2110.04607.

[19] E. Filippidi, D. G. DeMartini, P. M. De Molina, E. W. Danner, J. Kim, M. E. Helgeson, J. H. Waite, M. T. Valentine, The microscopic network structure of mussel (Mytilus) adhesive plaques, Journal of the Royal Society Interface (2015). doi:10.1098/rsif.2015.0827.

[20] P. J. Bishop, S. A. Hocknull, C. J. Clemente, J. R. Hutchinson, A. A. Farke, B. R. Beck, R. S. Barrett, D. G. Lloyd, Cancellous bone and theropod dinosaur locomotion. Part I-an examination of cancellous bone architecture in the hindlimb bones of theropods, PeerJ (2019). doi:10.7717/peerj.5778.

[21] N. E. Romijn, N. A. Fleck, The fracture toughness of planar lattices: Imperfection sensitivity, Journal of the Mechanics and Physics of Solids (2007). doi:10.1016/j.jmps.2007.04.010.

[22] C. Chen, T. J. Lu, N. A. Fleck, Effect of imperfections on the yielding of two-dimensional foams, Journal of the Mechanics and Physics of Solids (1999). doi:10.1016/S0022-5096(99)00030-7.

[23] H. C. Tankasala, V. S. Deshpande, N. A. Fleck, Tensile response of elastoplastic lattices at finite strain, Journal of the Mechanics and Physics of Solids (2017). doi:10.1016/j.jmps.2017.02.002.

[24] X. Geng, Y. Lu, C. Liu, W. Li, Z. Yue, Fracture characteristic analysis of cellular lattice structures under tensile load, International Journal of Solids and Structures (2019). doi:10.1016/j.ijsolstr.2019.01.006.

[25] H. Gu, M. Pavier, A. Shterenlikht, Experimental study of modulus, strength and toughness of 2D triangular lattices, International Journal of Solids and Structures 152-153 (2018) 207–216. doi:10.1016/j.ijsolstr.2018.06.028.

[26] A. Bhuwal, T. Liu, I. Ashcroft, W. Sun, Localization and coalescence of imperfect planar FCC truss lattice metamaterials under multiaxial loadings, Mechanics of Materials 160 (2021) 103996. doi:10.1016/j.mechmat.2021.103996.

[27] M. S. Pham, C. Liu, I. Todd, J. Lertthanasarn, Damage-tolerant architected materials inspired by crystal microstructure, Nature 565 (7739) (2019) 305–311. doi:10.1038/s41586-018-0850-3.

[28] C. Liu, J. Lertthanasarn, M. S. Pham, The origin of the boundary strengthening in polycrystal-inspired architected materials, Nature Communications (2021). doi:10.1038/s41467-021-24886-z.

[29] Y. Wang, O. Sigmund, Quasiperiodic mechanical metamaterials with extreme isotropic stiffness, Extreme Mechanics Letters (2020). doi:10.1016/j.eml.2019.100596.

[30] R. M. Latture, M. R. Begley, F. W. Zok, Design and mechanical properties of elastically isotropic trusses, Journal of Materials Research (2018). doi:10.1557/jmr.2018.2.

[31] M. C. Messner, Optimal lattice-structured materials, Journal of the Mechanics and Physics of Solids (2016). doi:10.1016/j.jmps.2016.07.010.

[32] O. Ibragimova, A. Brahme, W. Muhammad, J. Lévesque, K. Inal, A new ANN based crystal plasticity model for FCC materials and its application to non-monotonic strain paths, International Journal of Plasticity (2021). doi:10.1016/j.ijplas.2021.103059.

[33] D. Goldberg, Genetic algorithms in optimization, search and machine learning, Addison Wesley (1988).

[34] A. R. Conn, N. Gould, P. L. Toint, A globally convergent Lagrangian barrier algorithm for optimization with general inequality constraints and simple bounds, Mathematics of Computation (1997). doi:10.1090/s0025-5718-97-00777-1.

[35] B. Chopard, M. Tomassini, Particle swarm optimization, in: Natural Computing Series, 2018. doi:10.1007/978-3-319-93073-2_6.

[36] S. Kirkpatrick, C. D. Gelatt, M. P. Vecchi, Optimization by simulated annealing, Science (1983). doi:10.1126/science.220.4598.671.

[37] L. Keviczky, R. Bars, J. Hetthéssy, C. Bányász, Introduction to MATLAB (2019). doi:10.1007/978-981-10-8321-1_1.

[38] Y. L. Dong, B. Pan, A Review of Speckle Pattern Fabrication and Assessment for Digital Image Correlation, Experimental Mechanics (2017). doi:10.1007/s11340-017-0283-1.

[39] Y. Su, Z. Gao, Z. Fang, Y. Liu, Y. Wang, Q. Zhang, S. Wu, Theoretical analysis on performance of digital speckle pattern: uniqueness, accuracy, precision, and spatial resolution, Optics Express (2019). doi:10.1364/oe.27.022439.

[40] Y. Xu, H. Zhang, B. Šavija, S. Chaves Figueiredo, E. Schlangen, Deformation and fracture of 3D printed disordered lattice materials: Experiments and modeling, Materials and Design (2019). doi:10.1016/j.matdes.2018.11.047.

[41] N. a. Fleck, An overview of the mechanical properties of foams and periodic lattice materials, Cellular Metals and Polymers 2004 (2004).

[42] K. Hornik, M. Stinchcombe, H. White, Multilayer feedforward networks are universal approximators, Neural Networks (1989). doi:10.1016/0893-6080(89)90020-8.

[43] M. A. Bessa, R. Bostanabad, Z. Liu, A. Hu, D. W. Apley, C. Brinson, W. Chen, W. K. Liu, A framework for data-driven analysis of materials under uncertainty: Countering the curse of dimensionality, Computer Methods in Applied Mechanics and Engineering (2017). doi:10.1016/j.cma.2017.03.037.

[44] M. Mozaffar, R. Bostanabad, W. Chen, K. Ehmann, J. Cao, M. Bessa, Deep learning predicts path-dependent plasticity, Proceedings of the National Academy of Sciences 116 (52) (2019) 26414–26420.

[45] D. W. Abueidda, S. Koric, N. A. Sobh, H. Sehitoglu, Deep learning for plasticity and thermo-viscoplasticity, International Journal of Plasticity (2021). doi:10.1016/j.ijplas.2020.102852.

[46] F. Chollet, Deep Learning mit Python und Keras: Das Praxis-Handbuch vom Entwickler der Keras-Bibliothek, 2018.

[47] T. Moshagen, N. A. Adde, A. N. Rajgopal, Finding hidden-feature depending laws inside a data set and classifying it using neural network, arXiv preprint arXiv:2101.10427 (2021).

[48] D. P. Kingma, J. L. Ba, Adam: A method for stochastic optimization, in: 3rd International Conference on Learning Representations, ICLR 2015 - Conference Track Proceedings, 2015. arXiv:1412.6980.

[49] Y. E. Nesterov, A Method of Solving a Convex Programming Problem with Convergence Rate $\mathcal{O}(1/k^2)$, Soviet Mathematics Doklady (1983).

[50] J. Burgess, B. Gallagher, D. Jensen, B. N. Levine, MaxProp: Routing for vehicle-based disruption-tolerant networks, in: Proceedings - IEEE INFOCOM, 2006. doi:10.1109/INFOCOM.2006.228.

## Appendix A. Creation of face centre cubic quasi-disordered lattices

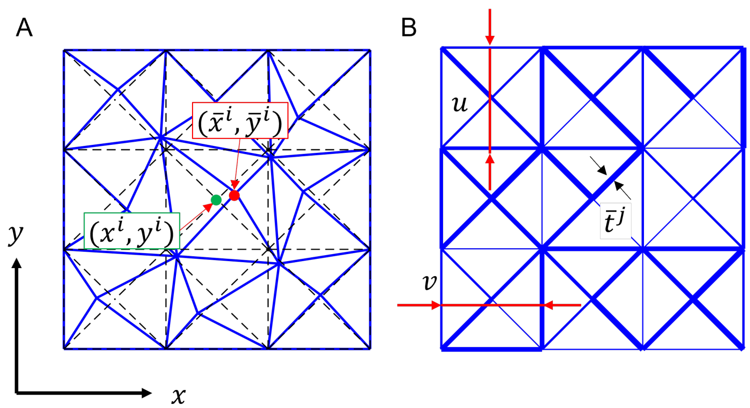


Figure A.1: Creation of FCC QTMs via (A) spatial coordinate perturbation (B) strut thickness variation.

In this section, we provide details to create FCC QTM designs. QTMs can be created via spatial coordinate perturbation of nodes, modelled by introducing geometrical perturbation to the nodes of a perfect FCC periodic lattice. Let $(x^i, y^i)$ represent the spatial coordinates of the $i$th node within a perfect FCC periodic lattice. The new position of the node $(\Delta x^i, \Delta y^i)$ after perturbation can be written as (Fig. A.1A):

$$\begin{aligned} \Delta x^i &= \bar{x}^i - x^i = \beta\alpha r \\ \Delta y^i &= \bar{y}^i - y^i = \beta\alpha r \end{aligned} \tag{A.1}$$

where $\beta\,(-1 \leq \beta \leq +1)$ denotes a random variable following a uniform probability distribution, $\alpha$ the degree of irregularity related to spatial coordinate perturbation, and $r$ the minimum distance between two nodes within the parent periodic FCC lattice, which can be calculated as:

$$r = \sqrt{\frac{u^2 + v^2}{4}} \tag{A.2}$$

where $u$ and $v$ are the lengths of the unit cell in the $x$ and $y$ directions of the parent periodic FCC lattice, respectively (Fig. A.1B). Instead, QTMs can be created via variation of strut thickness, $\bar{t}$, which, for the $j$th strut member, can be described as (Fig. A.1B):

$$\bar{t}^j = (1 + \gamma\beta)t^j \tag{A.3}$$

where $\gamma$ the degree of irregularity related to strut thickness variation. The possible 2D design spaces for QTMs are illustrated in Fig. A.2.

## Appendix B. Finite element modelling and damage model

Here, we present the details for FE modelling on the FCC lattices made of aluminium alloy Al-1050A. The lattice struts were represented as a 2-node Timoshenko-beam element (B21 in ABAQUS notation) with rigid connections. Each strut was modelled numerically as

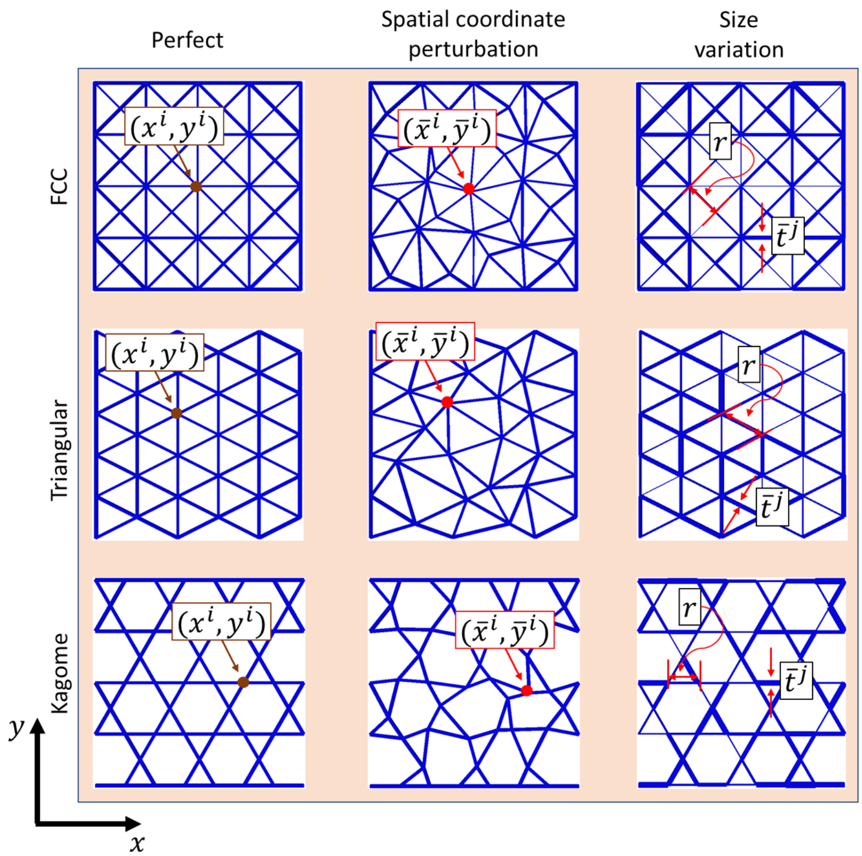


Figure A.2: The QTM design space for two-dimensional topologies

a uniform rectangular cross-sectioned solid bar of in-plane thickness, $t$, and unit out-of-plane width. For the parent periodic FCC lattice with identical lengths of the unit cell in the $x$ and $y$ directions, i.e., $u = v$, the relative density $\bar{\rho}$ of the perfect FCC lattice can be calculated as:

$$\bar{\rho} = 2\left(1+\sqrt{2}\right)\left(\frac{t}{v}\right) \tag{B.1}$$

The relative density value was kept at $\bar{\rho} = 0.2$ for all QTM topologies in our investigation. Simulation results suggested that converged results could be achieved with each strut meshed with ten beam elements of equal length. To simulate the uniaxial tensile experiment, the specimen was subject to a constant vertical displacement boundary condition on the top and a fixed boundary condition on the bottom, see Fig. B.1. The macroscopic stress $\Sigma$, and macroscopic tensile strain E were calculated as:

$$\begin{aligned} \Sigma &= \frac{\text{Reaction Force}}{W}, \\ \mathrm{E} &= \frac{\Delta L}{L} \end{aligned} \tag{B.2}$$

where $W$ and $L$ are the width and height of the QTMs, respectively; $\Delta L$ is the elongation

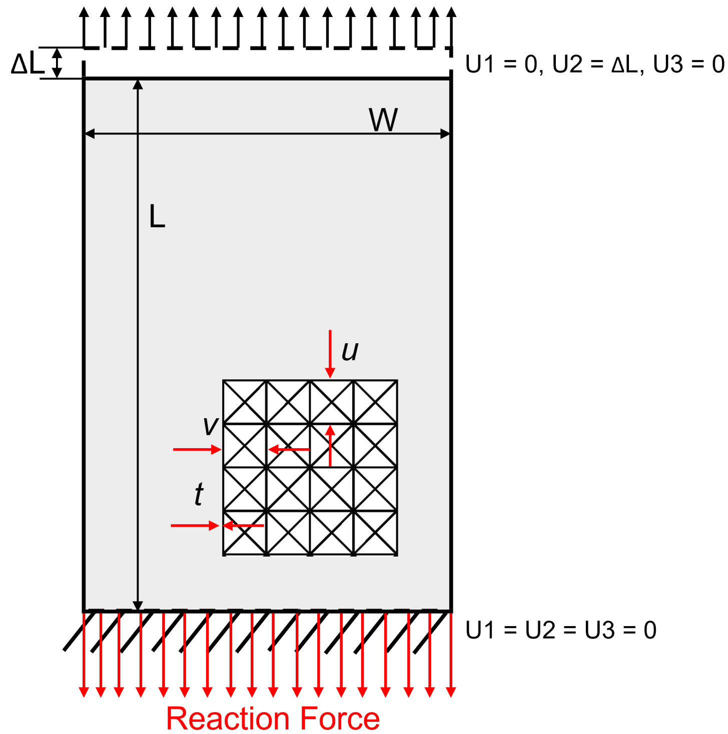


Figure B.1: The FE model of a typical metamaterial specimen

in the y-direction.

The Ramberg-Osgood model was used to represent the true stress-strain relationship of the parent material, i.e., Aluminium alloy Al-1050A, given by:

$$\bar{\varepsilon} = \frac{\bar{\sigma}}{\bar{E}} + \kappa \left( \frac{\bar{\sigma}}{\bar{\sigma}_y} \right)^{\eta} \tag{B.3}$$

where $\bar{E} = 70\text{GPa}$ and $\bar{\sigma_y} = 134\text{MPa}$ are Young's modulus and yield stress of the Aluminium alloy, respectively; $\kappa$ is the yield offset and $\eta$ is the hardening exponent [25].

Failure initiation starts when the maximum axial strain reaches 0.03 in the element based on the tensile test result shown in Fig. B.2 A [25]. The strut necking behavior is replicated by the reduction of the yield stress after failure initiates, which is characterised by the damage variable $D$:

$$\bar{\sigma} \;=\; (1 \;-D)\,\bar{\sigma_y} \tag{B.4}$$

where $D$ varies from 0 to 1, and is a function of the plastic strain, fitted to match the data of Fig. B.2A. The corresponding element is deleted from the mesh, when all the material points within the element failed ($D = 1$). Numerical validation was conducted against the experimental data based on a 2D triangular lattice reported by Huaiyuan et al. Fig. B.2 [25]. The FE prediction reported in this study shows a good agreement against the experimental data as shown in Fig. B.2 B. Additionally, Figs. B.2 C and D, show the comparison of failure loci of 2D triangular lattices given by Huaiyuan et al. [25] and numerical model used

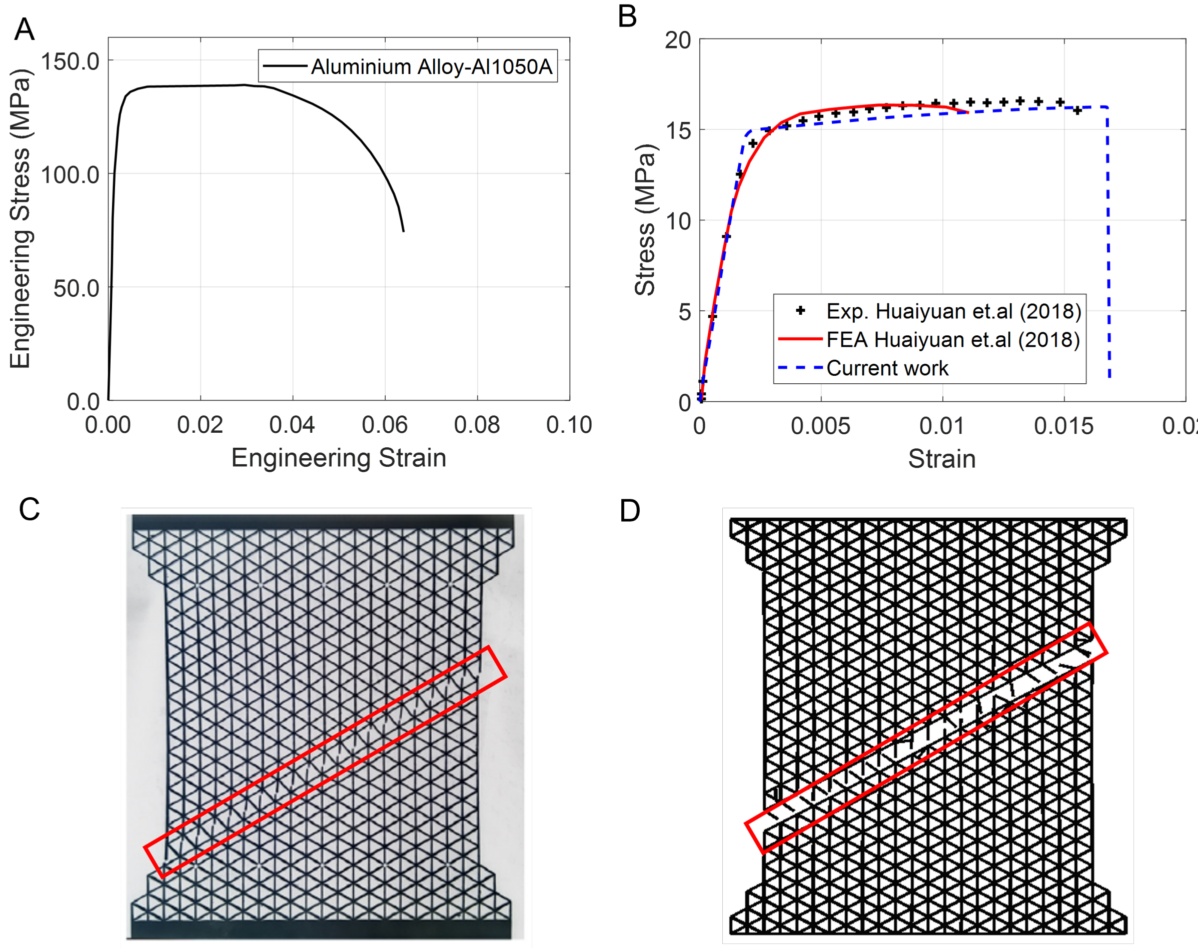


Figure B.2: (A) Engineering stress-strain curve of the aluminum alloy (Al1050A [25]) used for FE simulations, (B) Stress-strain response comparison and numerical validation against the experimental data based on a 2D triangular lattice reported by Huaiyuan et al. [25] (C and D) Single shear band fracture of 2D triangular lattice by experimental [25], and FE result of the current work, respectively.

in current study, respectively. This suggests that the FE simulation used in this study can achieve high fidelity.

## Appendix C. Artificial neural network

In recent studies, various ANN models are now being used. Among the suggested ANN types are multilayer perceptron feed-forward neural networks (FFNN), convolutional neural networks (CNN), and recurrent neural networks (RNN). Each ANN model generally relates to a specific type of issue. FFNN, for example, is widely utilized in many fields and is well-known as "universal approximators" [42–44]. Compared to CNN and RNN, FFNN has a simpler architecture (only layers and neurons in hidden layers are vulnerable to modification) and is thus easier to evaluate in its diversity. The current study has employed tabular data to relate the input dataset (spatial coordinate perturbations and strut thickness variations) to the relevant output dataset (normalized macroscopic stress-strain response). As a result, an FFNN with a backpropagation algorithm was adopted in this work, as shown in Fig. C.1A and B.

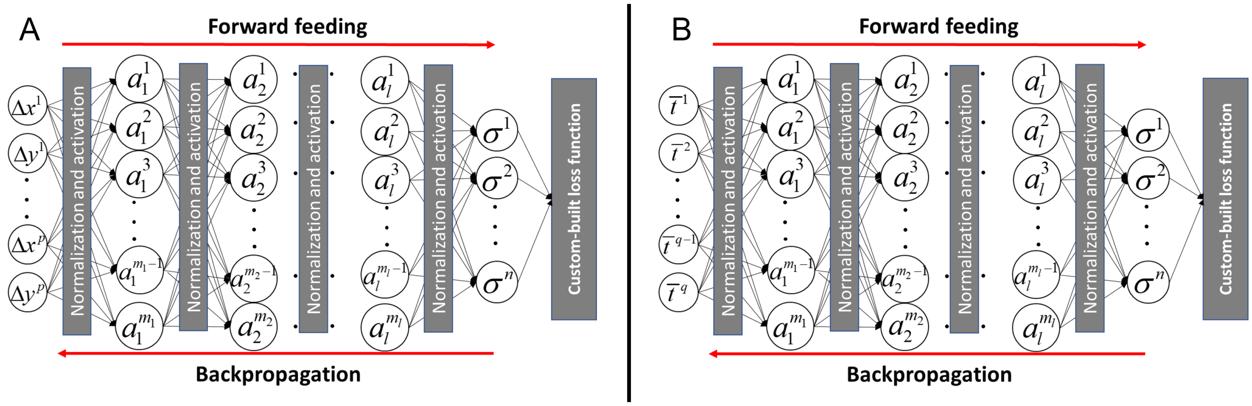


Figure C.1: An illustration of feed-forward neural network with backpropagation used in this work (A) spatial coordinate perturbation (B) strut thickness variation.

## Appendix C.1. Activation function and scaling

The rectified linear activation function (ReLU) was used in this study. ReLU has been widely used in feed-forward neural networks as an activation function [45]. In this work, the input was scaled between [-1, 1] for the spatial coordinate perturbation dataset and [0, 1] for the strut thickness variation dataset. The ReLU activation function was found to perform better with this scaling technique. To scale the $i$th input data, the following mathematical transformation was applied to it:

$$\Psi^{(i)}_{\text{norm. [-1 1]}} = 2\frac{\Psi^{(i)} - \min \Psi^{(i)}}{\max \Psi^{(i)} - \min \Psi^{(i)}} - 1, \quad \Psi^{(i)}_{\text{norm. [0 1]}} = \frac{\Psi^{(i)} - \min \Psi^{(i)}}{\max \Psi^{(i)} - \min \Psi^{(i)}}, \tag{C.1}$$

where $min\Psi^{(i)}$ is the minimum and $max\Psi^{(i)}$ is the maximum value of the $i$th component of the input vector $\boldsymbol{\Psi}$ in the dataset.

## Appendix C.2. Evaluation of ANN

The cost function, $J(\boldsymbol{\theta}^{[ii]}, \boldsymbol{b}_{ii})$, and loss function, $\mathcal{L}(\boldsymbol{\sigma}^m_{pred}, \boldsymbol{\sigma}^m_{true})$, are used to assess the "goodness" of the trained network. The loss function evaluates the model performance based on the real stresses, $\boldsymbol{\sigma}_{true} = [\sigma^1, \sigma^2, ..., \sigma^n]^{\mathrm{T}}_{true}$, and the predicted stresses, $\boldsymbol{\sigma}_{pred} = [\sigma^1, \sigma^2, ..., \sigma^n]^{\mathrm{T}}_{pred}$. During training, an optimisation algorithm minimises the value of the loss function by updating the weights and biases values in the "right" direction [46]. The cost function is dependent on the loss function in the following way:

$$J(\boldsymbol{\theta}^{[ii]}, \boldsymbol{b}_{ii}) = \frac{1}{h}\sum_{m=1}^{h} \mathcal{L}(\boldsymbol{\sigma}^m_{pred}, \boldsymbol{\sigma}^m_{true}) \tag{C.2}$$

where h is the number of samples in an evaluated dataset. The most commonly used loss function is the mean squared error (MSE) for regression analysis problems [47]. The equation is expressed as:

$$\mathcal{L}_{MSE}(\boldsymbol{\sigma}^m_{pred}, \boldsymbol{\sigma}^m_{true}) = \frac{1}{n}\sum_{k=1}^{n}\left(\sigma^k_{pred} - \sigma^k_{true}\right)^2 \tag{C.3}$$

The "logcosh" loss function for neural networks was developed to combine the advantage of the absolute error loss function of not overweighting outliers with the advantage of the mean square error of continuous derivative near the mean, which makes the last phase of learning easier, which can be expressed as:

$$\mathcal{L}_{\log\cosh}(\boldsymbol{\sigma}^m_{pred}, \boldsymbol{\sigma}^m_{true}) = \frac{1}{n}\sum_{k=1}^{n}\log(\cosh(\sigma^k_{pred} - \sigma^k_{true})) \tag{C.4}$$

As shown in Fig. C.2, numerical experiments on quasi-disordered FCC lattices have suggested that the stress data in the three groups (Zones) have significantly different variances across the QTM samples. Hence, we have proposed a custom-built loss function based on the "quantile regression loss function" to accurately predict stress-strain responses. The loss function used is given as:

$$\begin{aligned}\mathcal{L}_{custom}(\boldsymbol{\sigma}^k_{pred}, \boldsymbol{\sigma}^k_{true}) = \frac{1}{3n}\sum_{i=1}^{3}\Bigg[ & \sum_{\substack{k=1 \\ \sigma^k_{true}<\sigma^k_{pred}}}^{n} (\lambda_i - 1)\left(\sigma^k_{pred} - \sigma^k_{true}\right)^2 + \\ & \sum_{\substack{\mathrm{k=1} \\ \sigma^k_{true}\geq\sigma^k_{pred}}}^{n} \lambda_i\left(\sigma^k_{pred} - \sigma^k_{true}\right)^2\Bigg]\end{aligned} \tag{C.5}$$

where $\lambda_i$, $i = 1, ..., 3$, are the chosen quantiles for the three groups of the stress data and have values between 0 and 1. The quantile loss function is an extension of the Mean Square Error (MSE) that has the quantile $\lambda_i = 0.5$.

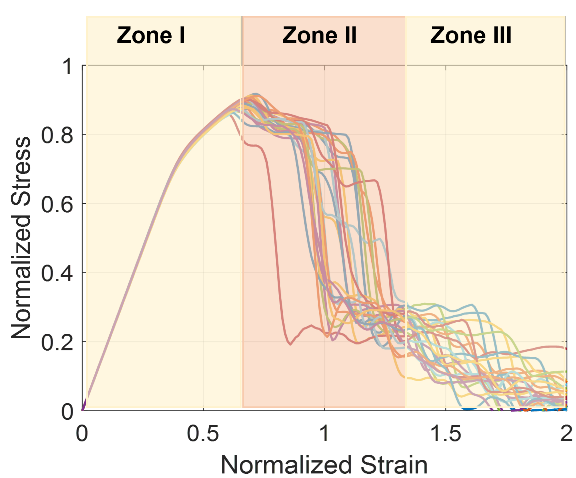


Figure C.2: Three zones in the stress-strain relation for the QTM samples under uniaxial tension.

### Appendix C.3. ANN Optimisation algorithm

Adaptive Moment Estimation (Adam) [48] is a widely used gradient descent-based back-propagation optimisation algorithm. In our study, this algorithm was used to train ANN models. For each parameter, the algorithm computes adaptive learning rates. It keeps an exponentially decaying average of previously squared gradients $\boldsymbol{\upsilon}_t$, like Nesterov's accelerated gradient method [49], MaxProp [50], and others. However, it differs in the way it updates an exponentially decaying average of past gradients:

$$\begin{aligned} \boldsymbol{\zeta}_t &= \omega_1 \boldsymbol{\zeta}_{t-1} + (1-\omega_1)\, g_t, \\ \boldsymbol{\upsilon}_t &= \omega_2 \boldsymbol{\upsilon}_{t-1} + (1-\omega_2)\, g_t^2, \end{aligned} \tag{C.6}$$

where $g_t$ the gradient; $\boldsymbol{\zeta}_t$ and $\boldsymbol{\upsilon}_t$ are approximations of the gradient's first moment (the mean) and second moment (the non-centred variance) at $t$th step. To compensate for moments that are biased towards zero, bias-corrected first and second moment estimates are computed:

$$\begin{aligned} \hat{\boldsymbol{\zeta}}_t &= \frac{\boldsymbol{\zeta}_t}{1-\omega_1^t} \\ \hat{\boldsymbol{\upsilon}}_t &= \frac{\boldsymbol{\upsilon}_t}{1-\omega_2^t} \end{aligned} \tag{C.7}$$

Eventually, parameters are updated according to:

$$\boldsymbol{\theta}_{t+1} = \boldsymbol{\theta}_t - \frac{\chi}{\sqrt{\hat{\boldsymbol{\upsilon}}_t} + \epsilon} \hat{\boldsymbol{\zeta}}_t \tag{C.8}$$

Where $\omega_1$, $\omega_2$, $\chi$, and $\epsilon$ are the algorithm hyperparameters and are subject to tuning.

### Appendix C.4. ANN architecture - hyperparameters

In this section, we have given the hyperparameters used to train our ANN model. Each ANN model received a total of 1000 training iterations. The initial learning rate, $\chi$, is 0.0009. It decreases by the factor 0.2427 when no training progress is made for 18 consecutive training epochs. The other optimizer hyperparameters were used as their default settings in MATLAB: $\omega_1 = 0.9$, $\omega_2 = 0.999$, and $\epsilon = 10^{-8}$ Early stopping was used for deep learning to stop training if the change in learning metrics did not exceed over ten consecutive training iterations. A batch size of 16 was used to train the networks. The hyperparameters to tune the neural networks are obtained using Bayesian optimization from MATLAB ('bayesopt') [37].

### Appendix C.5. ANN architecture analysis

To demonstrate an example of the improvements in the ANN architecture using our custom built loss function. The ANN model was analyzed based on hyperparameters mentioned above for the three loss functions mentioned in Eqs. C.3 to C.5. The geometries of 5000 QTM samples were used with irregularity, $\alpha = 0.2$, at constant relative density $\bar{\rho} = 0.2$. We used an ANN architecture consisting of 7 hidden layers with $4096, 2048, 1024, 1024, 1024, 512$, and 512 neurons, in sequence from input to output layers in our architecture. Further increase in hidden layers did not show any improvement in the efficiency of deep learning process. The dataset was split into three sub-datasets 75% for training, 15% for validations and 15% for

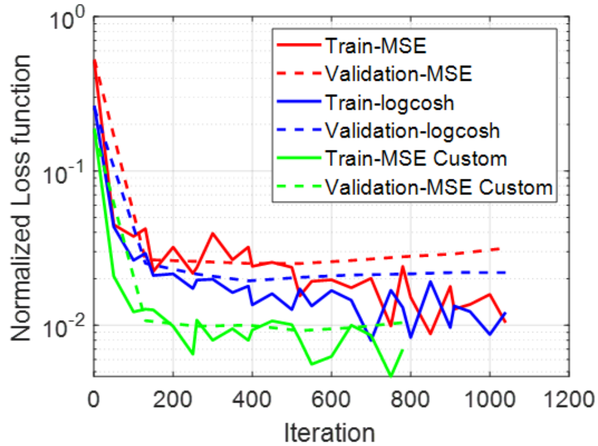


Figure C.3: The effects of loss functions on deep learning rate, which shows that the costom built loss function has the best performance.

tests. The evaluation of the three loss functions mentioned in Eqs. C.3 to C.5 are presented in the Fig. C.3 based on the training and validation datasets. It can be observed that, our custom-built loss function ($\lambda_1 = 0.5, \lambda_1 = 0.45$ and $\lambda_3 = 0.1$) has minimum loses compared to the other two loss functions (Eqs. C.3 and C.4).

Fig. C.4 compares the FEA with the ANN predictions of the stress-strain curves of the FCC QTMs generated via nodal perturbations ($\alpha = 0.2$). In the Fig. C.4, the first, second, and third row plots compare training, validation, and test datasets, respectively. The stress-strain curves are randomly selected from the respective datasets. Similarly, Fig. C.5 compares the FEA with the ANN predictions for FCC QTMs generated via strut thickness variations ($\gamma = 0.1$). In both cases good agreement has been achieved.

## Appendix D. Size effects of FCC QTMs

The size effects on the macroscopic stiffness, the macroscopic peak strength and ductility of the FCC QTMs were investigated using FE simulations. The details of the FE simulations are described in Appendix B. The QTMs were created based on the perfect FCC lattice with square unit cells (i.e., $u = v$). The width to height ratio, $W/L$, of the QTM samples were kept at 0.75; and the unit cell size, $v$, and the thickness, $t$, were taken as 10 mm and 0.4 mm, respectively. The size effects were evaluated by increasing the number of unit cells from 2 to 18 in $x$ direction. We have conducted FE simulations for 100 QTMs at relative densities of $\bar{\rho} = 0.2$ with nodal perturbation irregularity $\alpha = 0.2$ for each sample size. Fig. D.1A shows the size effect via the functional relationship of the structural macroscopic stiffness against the number of unit cells in $x$ direction. The macroscopic stiffness is not sensitive to the number of unit cells when number of cells were more than 12. As shown in Figs. D.1B and C, the peak strength and ductility converged at the lattice size of 12 unit cells in x-direction (i.e., 16 unit cells in $y$ direction). Thus, we opted for the QTMs of $12 \times 16$ unit cells for this methodology development, provided in the main text. The similar study has been conducted on strut thickness variability, the simulation results follow the same trend as shown in Fig. D.1.

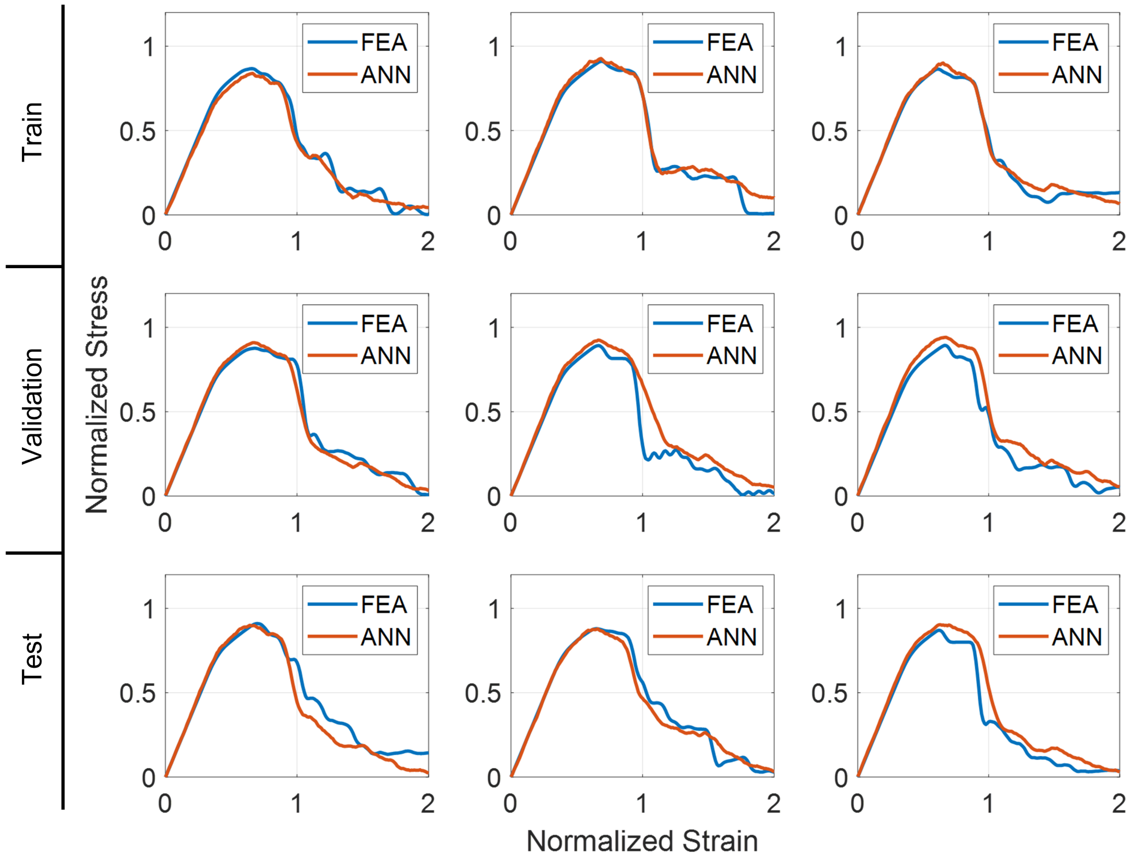


Figure C.4: The comparison of the FEA results with the ANN predictions for FCC QTMs generated via spatial coordinate perturbations.

## Appendix E. Stress-strain curves of polymers

Fig. E.1A shows the engineering stress-strain curves of *polymer1* and *polymer2* used in the experimental study. The optimized QTM design for the Experimental Study in the main text is manufactured using these two materials. A miniature specimen tensile tests were performed to get engineering stress-strain curves. The geometrical dimensions of the miniature sample are shown in Fig. E.1B. The detailed geometry used for tensile tests of the three selected FCC lattice designs, i.e., the parent periodic FCC lattice, the QTM with progressive failure mode (QTM-1), and the QTM with sudden failure mode (QTM-2) are given in Figs. E.2A, B and C, respectively.

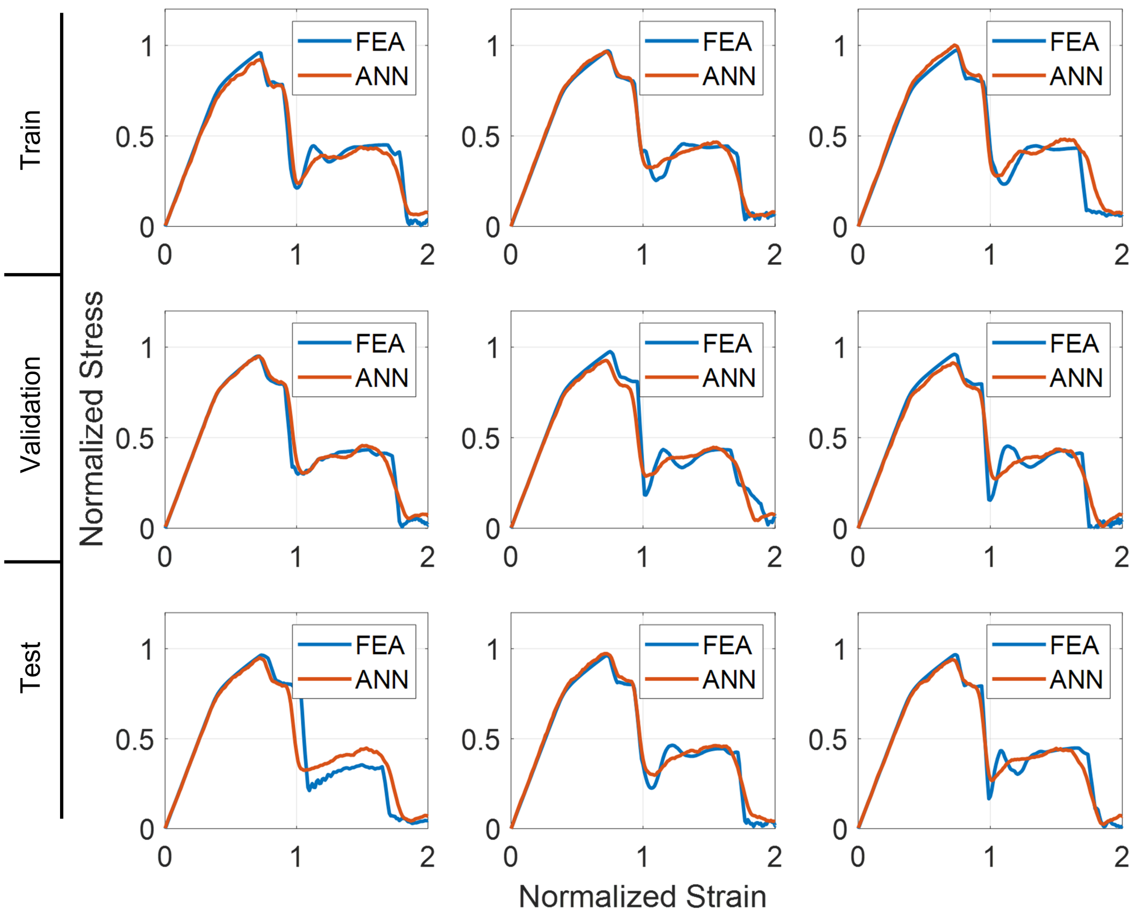


Figure C.5: The comparison of the FEA results with the ANN predictions for FCC QTMs generated via strut thickness variations.

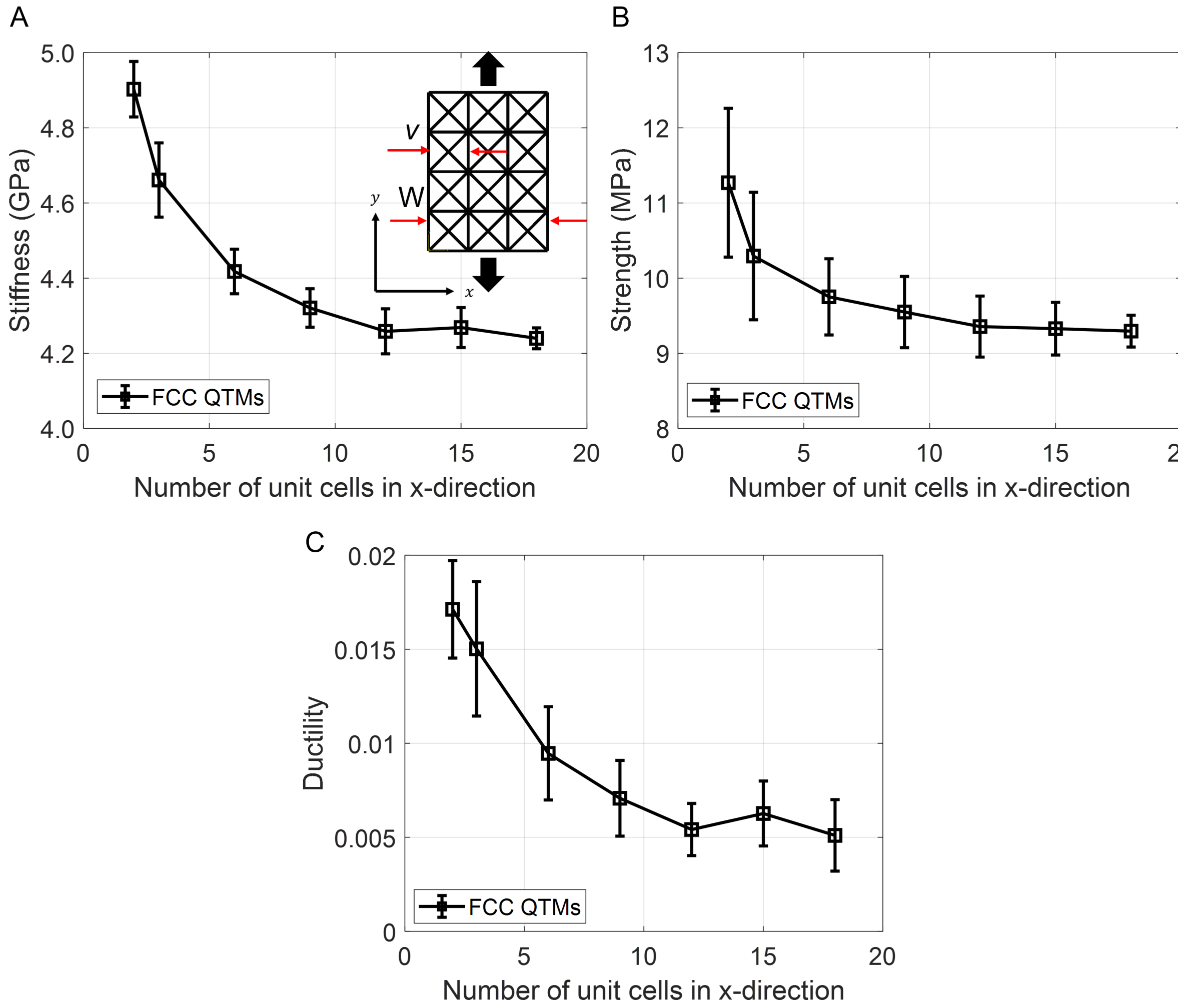


Figure D.1: The size effects on (A) the structural macroscopic stiffness, (B) the structural peak strength and (C) ductility of the FCC QTMs generated via spatial coordinate perturbations.

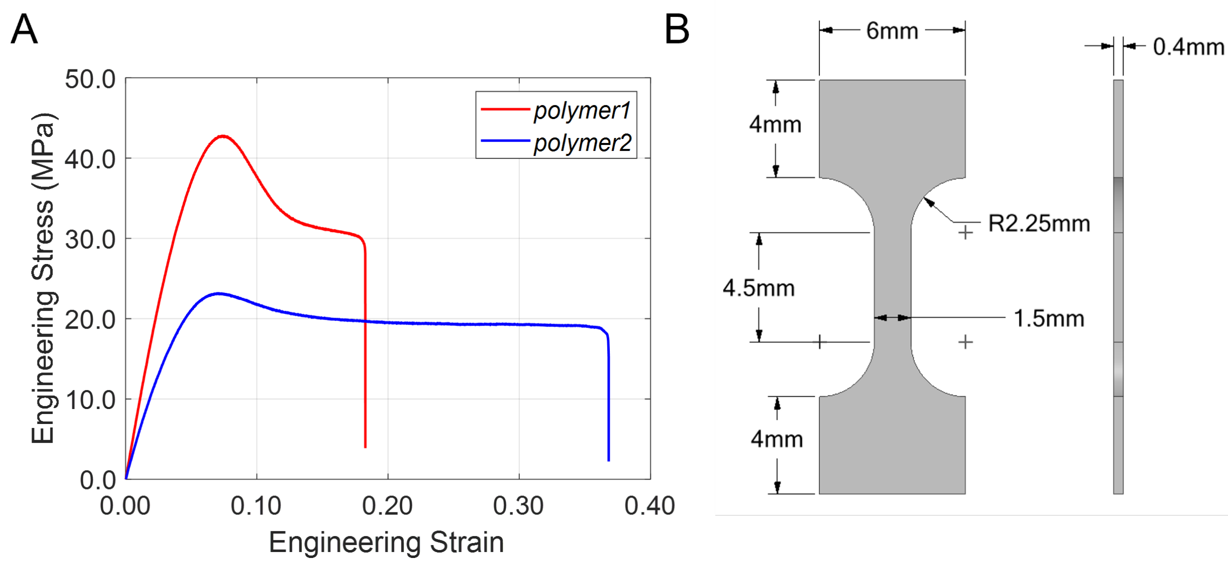


Figure E.1: (A) engineering stress-strain curves of the polymer1 amd polymer2; (B) miniature specimen dimensions.

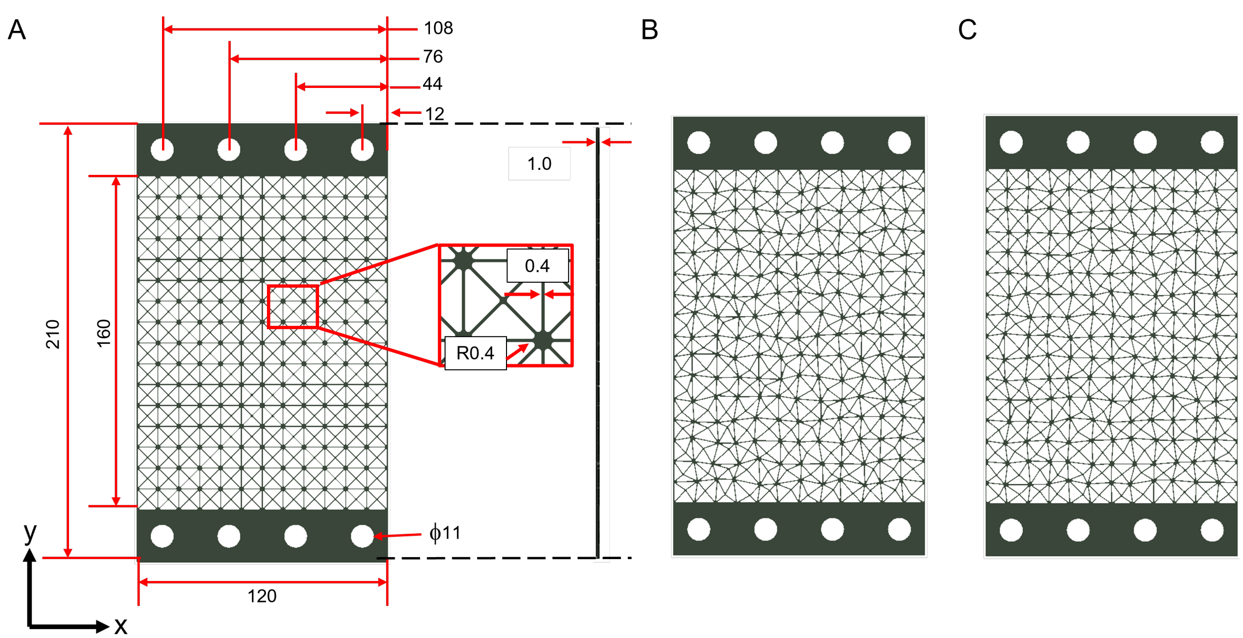


Figure E.2: Geometry details of (A) the parent periodic FCC lattice (B) the QTM with progressive failure mode (QTM-1) and (C) the QTM with sudden failure mode (QTM-2) used for uniaxial tensile test (all dimensions are in mm)